Crystal Structure of the Calcium Release–Activated Calcium Channel Orai

Xiaowei Hou, Leanne Pedi, Melinda M. Diver, Stephen B. Long*

The plasma membrane protein Orai forms the pore of the calcium release–activated calcium (CRAC) channel and generates sustained cytosolic calcium signals when triggered by depletion of calcium from the endoplasmic reticulum. The crystal structure of Orai from *Drosophila melanogaster*, determined at 3.35 angstrom resolution, reveals that the calcium channel is composed of a hexameric assembly of Orai subunits arranged around a central ion pore. The pore traverses the membrane and extends into the cytosol. A ring of glutamate residues on its extracellular side forms the selectivity filter. A basic region near the intracellular side can bind anions that may stabilize the closed state. The architecture of the channel differs markedly from other ion channels and gives insight into the principles of selective calcium permeation and gating.

In many cell types, the depletion of calcium ions (Ca^{2+}) stored within the endoplasmic reticulum (ER) causes the opening of Ca^{2+}-selective channels in the plasma membrane (*1*). The resulting influx of Ca^{2+} through these calcium release–activated calcium (CRAC) channels generates sustained intracellular Ca^{2+} signals, the roles of which are well appreciated in cells of the immune system, where they mediate signaling through B cell, T cell, and Fc receptors (*1*). Although this process of "store-operated Ca^{2+} entry" has been recognized for decades, Orai and stromal interaction molecule (STIM), the CRAC channel pore and its regulator, were identified fairly recently (*2*–*7*). Orai, located in the plasma membrane, forms the Ca^{2+} pore (*8*–*10*). Humans have three Orai proteins (Orai1 to -3). A mutation in Orai1 that renders the channel nonconductive [Arg^{91}→Trp^{91} (R91W) (*11*)] causes a form of immune deficiency, underscoring its importance in the immune system (*5*). STIM is a single-pass membrane protein in the ER that senses the luminal Ca^{2+} concentration. It opens the pore of Orai following Ca^{2+} store depletion, probably via interaction between the cytosolic portions of STIM and Orai, which accumulate at ER-plasma membrane junctions (*1*, *12*).

Orai proteins constitute a highly conserved ion-channel family and have no discernible sequence homology with other ion channels (*5*–*7*), suggesting distinctive architecture and mechanisms for selective ion permeation and gating. From sequence analysis, Orai is predicted to have four transmembrane helices (M1 to M4). The chemical accessibility and intersubunit cross-linking of cysteine residues introduced into the channel by mutagenesis predict that residues on the M1 helix contribute to the ion-conduction pore (*13*, *14*). Several lines of evidence indicate that Orai channels are multimers, but studies have led to differing conclusions about the oligomeric state. Some studies suggest a tetrameric assembly (*15*–*18*), whereas others hint at a higher-order oligomer (*14*) or raise the possibility that the oligomeric state of the channel might change when it is activated by STIM (*15*, *18*).

Under physiological conditions, in which the extracellular Ca^{2+} concentration is 1 to 2 mM, CRAC channels select for Ca^{2+} over monovalent cations such as sodium (Na^+) or potassium (K^+) by more than 1000:1, placing them among the most highly-selective Ca^{2+} channels known (*19*). However, as is the case for many Ca^{2+}-selective channels, when divalent cations are removed from the extracellular solution, CRAC channels become permeant to monovalent cations, including K^+ and Na^+ (*19*, *20*). Both the Ca^{2+} and monovalent cation currents through CRAC channels require activation by STIM and are blocked by gadolinium (Gd^{3+}) and lanthanum (La^{3+}) ions from the extracellular side (inhibition constant K_i < 100 nM) (*8*, *21*, *22*).

To better understand ion permeation, ion selectivity, and gating in CRAC channels, we have determined the crystal structure of Orai from *Drosophila melanogaster*, which shares 73% sequence identity with human Orai1 within its transmembrane region. We have also determined the structure of the nonconductive K163W mutant, corresponding to the R91W mutant in Orai1 that causes immune deficiency in humans. The structures define the architecture of a Ca^{2+} channel, establish principles of its Ca^{2+} selectivity, and give insight into the mechanism of activation by STIM.

Structure determination and channel reconstitution. To obtain well-diffracting crystals of Orai, we evaluated the biochemical behavior of

Structural Biology Program, Memorial Sloan-Kettering Cancer Center (MSKCC), 1275 York Avenue, New York, NY 10065, USA.

*To whom correspondence should be addressed. E-mail: longs@mskcc.org

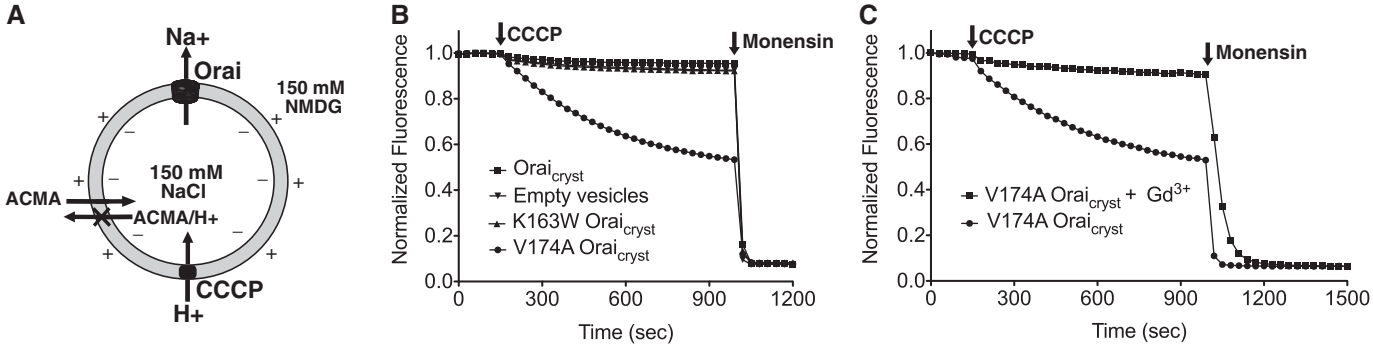

Fig. 1. Channel reconstitution in liposomes. (**A**) Schematic of the fluorescence-based flux assay. Vesicles containing Orai or those prepared without protein (empty vesicles) were loaded with 150 mM NaCl and diluted 100-fold into flux buffer containing a fluorescent pH indicator (ACMA) and 150 mM *N*-methyl-D-glucamine (NMDG) to establish a Na^+ gradient. After stabilization of the fluorescence signal (150 s), a proton ionophore (CCCP) was added to the sample, and an electrical potential arising from Na^+ efflux was used to drive the uptake of protons into the vesicles, which quenches the fluorescence of ACMA. The "X" indicates that ACMA is no longer membrane-permeable in the protonated form. (**B**) Fluorescence measurements for the indicated protein constructs of Orai. Monensin, a Na^+ ionophore, was added after 990 s to render all vesicles permeable to Na^+ and establish a minimum fluorescence baseline. Fluorescence was normalized by dividing by the initial value. (**C**) Fluorescence trace observed for V174A Orai$_{cryst}$ in the absence and presence of Gd^{3+}.

~50 orthologs and engineered a variety of protein forms, including truncations and fusions. Crystals that diffracted to 3.35 Å resolution were obtained from a construct (termed $Orai_{cryst}$) spanning residues 132 to 341 of Orai from *Drosophila melanogaster* in which two nonconserved cysteine residues and two residues in the hypervariable M3-M4 loop were mutated (see the supplementary materials and methods). The construct corresponds to the conserved region of Orai and contains all regions necessary for activation by STIM (fig. S1) (*23*–*25*).

We tested the function of the purified channel protein by reconstituting it into liposomes and using a fluorescence-based assay to monitor ion flux under divalent ion-free conditions (Fig. 1). As would be expected for a closed channel before activation by STIM, ion flux was not detected for $Orai_{cryst}$ or for the K163W mutant. Introduction of the mutation V174A (V102A in Orai1), which creates channels that are open in the absence of STIM (*26*), yielded a robust decrease in fluorescence, indicative of ion flux (Fig. 1B). We confirmed that the fluorescence decrease was due to ion flux through Orai by adding the pore-blocker Gd^{3+}, which eliminated the observed flux through the pore but had no effect on the baseline fluorescence induced by the Na^{+}-ionophore monensin (Fig. 1C). Therefore, the reconstituted protein recapitulated known properties of Orai.

The crystals form in the space group $P2_13$ and contain two Orai subunits (referred to as subunits A and B of the channel) within the asymmetric unit. Experimental phases were derived from diffraction data collected from crystals containing mercury, iridium, and gadolinium heavy atoms. The phases, which were improved by noncrystallographic symmetry averaging, yielded an electron-density map that allowed placement of the majority of the amino acid side chains (fig. S2). The atomic model contains amino acids 144 to 334 of Orai, except for the M1-M2 loop (amino acids 181 to 190), the M2-M3 loop (amino acids 220 to 235), and amino acids 330 to 334 of subunit B, which are disordered. Anomalous-difference electron-density peaks for sulfur atoms of methionine and cysteine residues confirm the correct assignment of amino acids in the atomic model (fig. S2E), which is refined to a free residual (R_{free}) of 28% (table S1).

Architecture of Orai. The crystal structure shows that the channel is formed from a hexamer of six Orai subunits arranged around a central axis (Fig. 2). Cross-linking and light-scattering data are consistent with a hexameric assembly for both purified Orai in detergent and Orai expressed in cell membranes (fig. S3). Each subunit contains four transmembrane α helices (M1 to M4) and a helix following M4 that extends into the cytosol (termed the M4 extension helix). The M4 extension helices of neighboring subunits adopt one of two alternating conformations and pack with each other in pairs, giving this region of the channel threefold symmetry (Fig. 2). Within the channel's transmembrane region, there is sixfold symmetry.

The ion pore is located at the center of the channel along the sixfold axis, and the transmembrane helices are arranged in three concentric rings (Fig. 2B). Six M1 helices, one from each subunit, make up an inner ring of helices and line the ion pore. The M2 and M3 helices constitute a middle ring that surrounds the transmembrane portion of the M1 helices and separates them from M4 helices, which are arranged in an outer ring and located at the periphery of the channel. The channel extends just beyond the extracellular side of the membrane, and the M1 helix and the M4 extension helix protrude 20 to 25 Å into the cytosol.

The M1 helices extend from Thr^{144} to Gln^{180} and are ~55 Å long. The region of M1 that extends into the cytosol was not expected to be part of M1 from sequence analysis and includes four helical turns at its N terminus (residues 144 to 157). As this region does not make contacts with other parts of the channel in the structure, it could conceivably interact with cellular factors such as STIM.

The M2 helix traverses just beyond the thickness of a lipid bilayer, and the M3 helix extends about two helical turns further into the cytosol. The arrangement of the M2 and M3 helices in a ring surrounding the transmembrane portion of the M1 helices, while leaving the cytosolic portion of M1 free, suggests that M2 and M3 help provide structural integrity to the transmembrane region of the pore but would permit widening of the intracellular region of the pore.

The M4 helices are located furthest away from the ion pore. In comparison to the M1 to M3 helices, the M4 helices have fewer contacts with other parts of the channel, and their peripheral location may allow mobility (Fig. 2A). A bend near the middle of the transmembrane region (Pro^{288}) means that approximately half of M4 (within the outer leaflet) is roughly perpendicular to the plane of the membrane, whereas the other half is oriented diagonally (Fig. 2A). Connected to M4 by a highly conserved hinge region (residues 305 to 308), the M4 extensions of subunit A and subunit B pair with one another through an antiparallel coiled-coil helix packing arrangement (Fig. 2C). The interaction involves two residues from each subunit (Ile^{316} and Leu^{319}) that form a hydrophobic patch on the M4 extension, which is otherwise predominantly decorated with hydrophilic amino acids. Mutation of either residue (L273S or L276D mutants of Orai1) disrupts interaction with STIM and its ability to open the channel (*27*–*29*).

Chemical composition of the pore. The chemical environment along the length of the ion pore

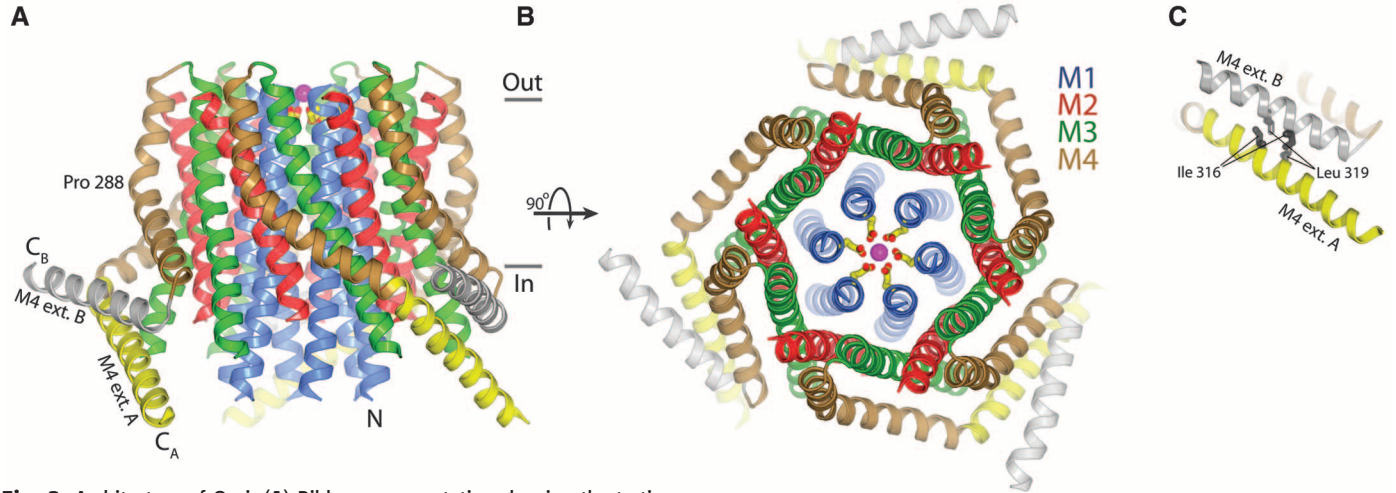

Fig. 2. Architecture of Orai. (**A**) Ribbon representation showing the tertiary structure of the channel from the side. The helices are colored: M1 (blue), M2 (red), M3 (green), M4 (brown), M4 extension (yellow in subunit A and gray in subunit B). Also shown are a Ca^{2+} ion (magenta sphere) and the nearby Glu^{178} residues (yellow sticks). Based on the hydrophobic region of the channel's surface, horizontal lines (~30 Å apart) suggest approximate boundaries of the inner (In) and outer (Out) leaflets of the membrane. (**B**) Orthogonal view of the channel from the extracellular side. (**C**) Close-up view showing the interaction between the M4 extension helices.

is determined by side chains of the amino acids of M1 that line the pore. This is in marked contrast to the pore of K^+ channels, where a substantial part of it is formed by an extended conformation of the polypeptide backbone (*30*). The pore of Orai has four distinct sections (Fig. 3, A and B): (i) a ring of glutamates at its extracellular end (termed the glutamate ring and composed of six Glu^{178} side chains), (ii) a hydrophobic section spanning three helical turns of M1 within the transmembrane region, (iii) a basic section spanning three helical turns near the intracellular side, and (iv) a wider section that extends into the cytosol.

The pore is ~55 Å long, and its diameter varies along its distance (Fig. 3B). In the glutamate ring, the Glu^{178} side chains point toward the center of the pore with their side chain oxygen atoms separated by ~6 Å across the pore, giving the extracellular entrance to the pore negative electrostatic potential (Fig. 3, B and C). Glu^{178}, which is conserved in Orai channels, is the only acidic residue lining the pore (*31*).

The side chains of Val^{174}, Phe^{171}, and Leu^{167} are separated by 8 to 10 Å across the pore and line the walls of the hydrophobic section, which is roughly tube-shaped and ~18 Å long (Fig. 3B). The hydrophobic side chains are well packed in the pore, make extensive van der Waals interactions with one another, and are strictly conserved among Orai channels. This region also has well-defined electron density (fig. S2) and the lowest temperature factors of the structure, suggesting that it is relatively rigid. In addition to lining the pore, the hydrophobic residues form a core of the protein that likely contributes to the channel's structural integrity. Mutations of amino acids in the hydrophobic region have yielded channels with dramatically altered ion-conduction properties. For instance, mutations of Val^{174} (Orai1 mutants V102C, V102A, V102T, or V102S) or Gly^{170} (Orai1 mutants G98P and G98D), which closely packs its Cα carbon with the side chain of Phe^{171}, result in channels that are constitutively conductive and demonstrate altered ion selectivity (*26*, *32*). The close packing in the hydrophobic region suggests that the functional abnormalities of these mutants may be due to reduced structural integrity and/or slightly altered packing in the pore.

Below the hydrophobic region in Fig. 3B and near the intracellular side of the membrane, the pore is lined by three basic residues from each subunit (Lys^{163}, Lys^{159}, and Arg^{155}) that are conserved as lysine or arginine among Orai orthologs (fig. S1). The 18 lysine or arginine residues that line this portion of the pore create an unexpected environment for the pore of a channel that conducts cations (Fig. 3D). The M1 helix is slightly bent at Ser^{162} and is enriched for residues that are often associated with bends in helices (serine, threonine, and glycine) in the region that spans the junction between the hydrophobic and basic portions of the pore (Fig. 3A and fig. S4). This raises the possibility that the conformation of the basic region could change, perhaps as part of the gating process, while the hydrophobic section and glutamate ring remain fairly fixed.

External Ca^{2+} binding and ion selectivity. In crystals soaked in Ca^{2+}, electron density consistent with a Ca^{2+} ion is observed on the extracellular side of the glutamate ring (in what we term the external site) (Fig. 4A). Because it is difficult to distinguish Ca^{2+} from other ions or water molecules in electron-density maps, we collected diffraction data from a crystal soaked in barium (Ba^{2+}), which permeates through the CRAC channel (*22*, *33*) and can be identified in electron-density maps from its anomalous diffraction signal. The anomalous-difference electron-density map contained a 10σ peak for Ba^{2+} in the external site, consistent with the assessment that it is a binding site for Ca^{2+} (Fig. 4A). Ba^{2+} is positioned slightly farther away from the glutamate ring than Ca^{2+}, and this correlates with the ionic radii of the ions (1.35 Å for Ba^{2+} and 0.99 Å for Ca^{2+}). It is possible that the ion coordination, which could be either direct or water-mediated, is not sixfold symmetric due to the flexibility of glutamate side chains. The backbone carbonyl oxygen of Glu^{178} at the C-terminal end of M1 might also contribute to Ca^{2+} binding (Fig. 4A). To investigate if Gd^{3+} blocks the channel by binding to the same site, we collected diffraction data from crystals soaked in Gd^{3+}, which also has a strong anomalous diffraction signal. The anomalous-difference electron-density map showed a 14σ peak for Gd^{3+} in the external site (Fig. 4B). The density is positioned closer to the glutamate ring than for Ca^{2+}; this

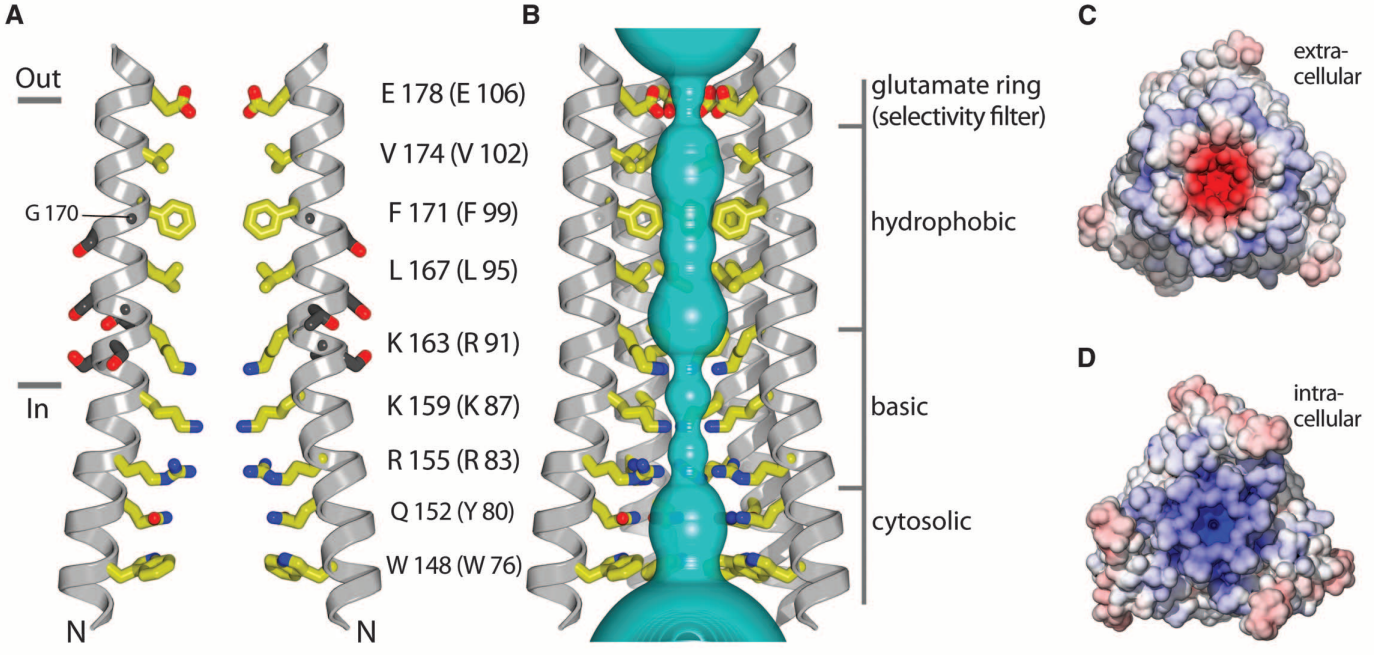

Fig. 3. Ion pore. (**A**) Two M1 helices are drawn (four are omitted for clarity), showing the amino acids lining the pore in yellow. The approximate boundaries of the membrane-spanning region are shown as horizontal lines. The corresponding amino acids in human Orai1 are shown in parentheses. Ser^{161}, Ser^{162}, Thr^{164}, Ser^{165}, Ser^{169}, and Gly^{170} are drawn as gray sticks. (**B**) View of the pore. Within a ribbon representation of four M1 helices (two in the foreground are removed for clarity) is a representation (teal) of the minimal radial distance from the center to the nearest van der Waals protein contact. The sections of the pore discussed in the text are labeled. (**C** and **D**) Molecular surface of Orai viewed from the extracellular (C) and intracellular (D) sides and colored according to the electrostatic potential contoured from −10 kT (red) to +10 kT (blue) (dielectric constant: 80).

may be indicative of the high affinity of Gd^{3+} and its +3 charge. Notably, the single Ca^{2+} binding site identified is located just outside the pore rather than within it. This configuration of ion binding distinguishes Orai from K^+ channels, which have multiple ions present within the pore in their structures (*34*), and this probably reflects differences in the mechanisms for ion permeation and selectivity.

CRAC channels may achieve their exquisite Ca^{2+} selectivity by high-affinity binding of Ca^{2+} to the glutamate ring that probably constitutes the ion selectivity filter. Accordingly, mutation of the glutamate (Glu^{178} in Orai or Glu^{106} in Orai1) to aspartic acid dramatically increases the channel's permeability to monovalent cations (*8–10*, *13*). Because the ionic radii of Ca^{2+} and Na^+ are nearly identical (0.99 and 0.95 Å, respectively), selectivity for Ca^{2+} is most likely due to the ion's greater positive charge. Consistent with this trend, we observe that high-affinity blockage of Orai by the trivalent lanthanide Gd^{3+} is due to binding in the external site.

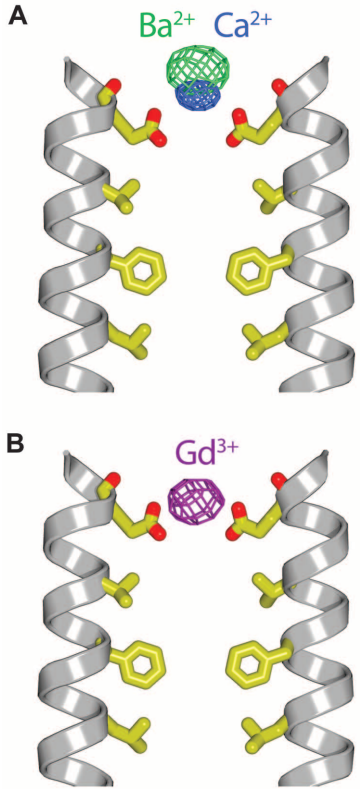

Fig. 4. Cation binding in the external site. (**A**) Ba^{2+} and Ca^{2+} binding. The glutamate ring and hydrophobic section of the pore are depicted as in Fig. 3A. Anomalous-difference electron density for Ba^{2+} is shown in green mesh (calculated from 20 to 5 Å resolution using phases derived from the final model and contoured at 6σ from a diffraction data set collected from a crystal soaked in 50 mM $BaCl_2$ using x-rays with λ = 1.70 Å. Electron density corresponding to Ca^{2+} is shown from a simulated annealing F_o-F_c omit map (blue mesh, calculated from 20 to 3.8 Å resolution and contoured at 4σ) from a crystal soaked in 50 mM $CaCl_2$ (table S1). The backbone carbonyl oxygen of Glu^{178} is also shown in stick representation. (**B**) Gd^{3+} binding. Anomalous-difference electron density is shown in purple mesh from a crystal soaked in 1 mM $GdCl_3$ (calculated from 20 to 5 Å resolution using model phases and contoured at 11σ from a diffraction data set collected using λ = 1.70 Å x-rays).

Identification of the external site raises the question of whether there is only one Ca^{2+} binding site or if there are other site(s) that are occupied during permeation. In Orai, the Ca^{2+} permeation rate [up to ~10^4 ions per second (*35*, *36*)] is much slower than the rate at which Ca^{2+} ions would diffuse to the extracellular mouth of the pore [~10^6 ions per second at physiological Ca^{2+} concentration (*37*)], so a single high-affinity Ca^{2+} binding site with a fast on-rate (from the extracellular solution) and a slow off-rate (into the pore) might be able to account for Ca^{2+}-selective permeation. However, some evidence, including an anomalous mole fraction effect (*33*), suggests that there may be more than one Ca^{2+} binding site. A second binding site might account for the property that, although Na^+ currents through CRAC channels are blocked by micromolar concentrations of Ca^{2+}, Ca^{2+} does not appreciably flow until the external solution contains millimolar concentrations of it (*19*, *20*). Additionally, the extent of blockage of Na^+ current at micromolar levels of Ca^{2+} is dependent on the voltage applied across the membrane (~10% block at –20 mV and ~50% block at –80 mV with 20 μM external Ca^{2+}) (*36*, *38*), which suggests that an ion binding site is located within the voltage gradient, whereas the external site would probably be located outside of it.

If a second binding site for Ca^{2+} in the selectivity filter exists, we expect that it would be located just below the glutamate ring. This hypothetical internal site, which might only be occupied transiently during permeation, would reside within a voltage field across the membrane and may explain the voltage-dependence for blockage of Na^+ current by Ca^{2+}. The binding of a Ca^{2+} ion in the external site could displace a Ca^{2+} ion from the internal site due to electrostatic repulsion between the ions, thereby allowing selective Ca^{2+} permeation.

Anion binding in the basic region of the pore. Electron-density maps have strong density in the basic region of the pore that appears to plug it. The anomalous-difference electron density was also strong in this site (up to 20σ), aiding the identification of the bound atom(s) (Fig. 5A). The density cannot be due to the surrounding protein side chains because they would have negligible anomalous scattering, and the components of the crystallization solution did not contain elements that would give a strong anomalous signal. To identify possible metal ions that might have copurified with Orai, purified protein was analyzed by inductively coupled plasma mass spectrometry (ICP-MS) and found to contain ~0.6 molar equivalents of iron and ~0.1 molar equivalents of zinc (table S2), both of which have anomalous scattering properties. Diffraction data collected using x-rays with a wavelength (λ) of 1.735 Å, slightly shorter than an absorption edge for iron (1.7433 Å) where the anomalous signal from iron would be strong (the imaginary component of the anomalous scattering factor f'' for iron is approximately 3.9 electrons at λ = 1.735 Å), yielded a 20σ peak in the anomalous-difference map (Table 1). Using λ = 1.900 Å x-rays, where the anomalous signal from iron would be weaker (f'' ~ 0.5 electrons), the peak was 5σ. F_o-F_c electron-density maps calculated from these data sets had comparable (~10σ) peaks, indicating that the difference in the strength of the anomalous signal was not due to differing occupancies of the bound entity between the crystals. Data sets collected above and below an absorption edge for zinc (λ = 1.284 Å) yielded comparable anomalous-difference density in the pore, but indicated that zinc was bound in a crystal contact (fig. S6). We therefore conclude that a major species bound in the basic region of the pore contains iron, which was present in the media used for cell growth.

Because this region of the pore is highly basic, we tested whether it could bind anions by soaking crystals in the complex anion iridium hexachloride, $(IrCl_6)^{3-}$. Diffraction data were collected using λ = 1.1033 Å x-rays to optimize the anomalous diffraction signal from iridium (f'' ~ 10.1 electrons), where it would be stronger than that for iron (f'' ~ 1.8 electrons) (Table 1). The anomalous-difference electron-density map contained two peaks in the basic region: (i) a 29σ peak for $(IrCl_6)^{3-}$ between Lys^{163} and Lys^{159} and (ii) an 8σ peak adjacent to Arg^{155} (Fig. 5B). Otherwise, the overall structure of Orai complexed with $(IrCl_6)^{3-}$ was indistinguishable from the native structure. We conclude that the basic region can bind anion(s). Because we observe iron in this anion binding site, we speculate that it is also bound in the form of a complex anion or mediated by counter ions. In support of this, hexachloroferrate anions, $(FeCl_6)^{3-}$, are known to be stabilized by hydrogen-bond interactions with amines (*39*). Although possible, it seems unlikely that iron binds within the pore in a physiological setting because of the limited amount of iron freely available within cells. More likely, the basic region of the pore binds available intracellular anion(s), with possible candidates being a sulfate or phosphate species (phosphate, pyrophosphate, etc.).

The K163W mutant. The crystal structure of the nonconductive K163W mutant gives further insight into the basic region of the pore. The overall structure of the K163W mutant is indistinguishable (at the current resolution) from the structure with the wild-type (WT) pore (root mean square deviation for Cα atoms is 0.1 Å). The only discernible difference with regard to the protein is that the side chain of the tryptophan residue at position 163 projects into the pore (Fig. 5C). The

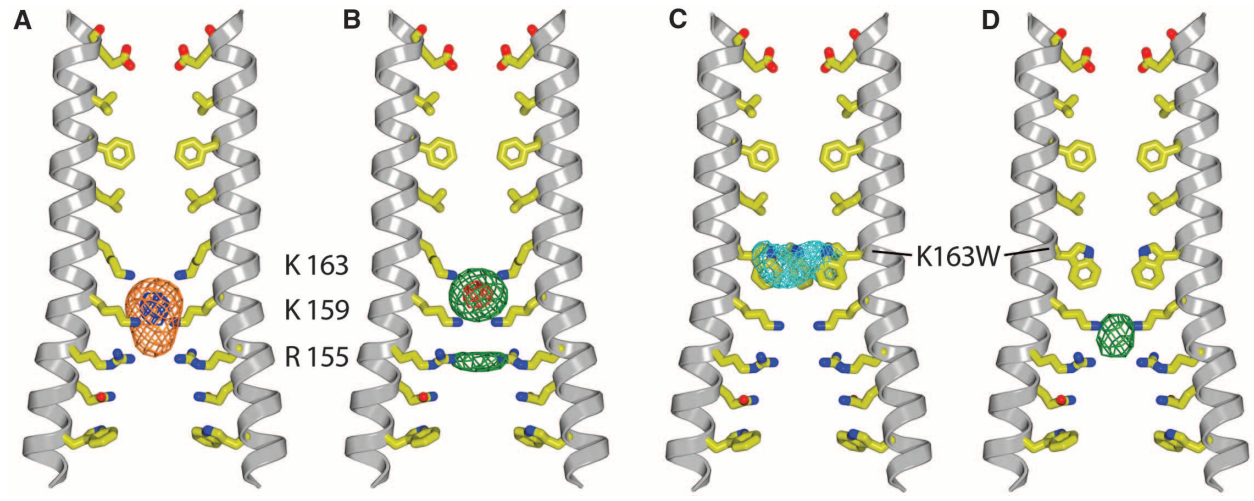

Fig. 5. Anion binding and the K163W mutant. (**A**) Anomalous-difference electron density in the basic region of the WT pore contoured at 7σ (orange mesh) and 14σ (blue mesh) from a native unsoaked crystal. The M1 helices are depicted as in Fig. 3A. The map was calculated using phases derived from the protein model and a diffraction data set collected using λ = 1.735 Å x-rays (resolution range 20 to 5 Å) (Table 1). (**B**) Anomalous-difference electron density present in the WT pore from a crystal soaked in $(IrCl_6)^{3-}$. The map is contoured at 7σ (green mesh) and 20σ (red mesh) (calculated using model phases from 20 to 5 Å resolution from a diffraction dataset collected using λ = 1.1033 Å x-rays). (**C** and **D**) The K163W mutant. Two M1 helices of the K163W mutant are depicted in the same manner as in (A). (C) Electron density (cyan mesh) is shown for the tryptophan side chains at residue 163 (represented as sticks). The density is from a simulated annealing F_o-F_c map in which the tryptophan side chains have been removed from the model (calculated from 20 to 3.35 Å resolution and contoured at 3σ). (D) Anomalous-difference electron density (green mesh) in the pore of a K163W mutant crystal soaked in $(IrCl_6)^{3-}$ (calculated from 20 to 5 Å resolution using model phases and contoured at 7σ from a diffraction data set collected using λ = 1.1033 Å x-rays).

six tryptophan residues, one from each subunit, are tightly packed and extend the hydrophobic region of the pore an additional helical turn.

Electron-density maps for the K163W mutant did not contain the anomalous-difference density within the pore ascribed to iron. Accordingly, ICP-MS analysis of the K163W mutant protein indicated that it contains only about one third as much iron (table S2). Lys^{159} and Arg^{155} have less well-defined electron density in the mutant, presumably due to the absence of an anion. To explore the effect of the K163W mutant on the ability of the pore to bind anions, we calculated an anomalous-difference electron-density map from a crystal soaked in $(IrCl_6)^{3-}$ and found that its distribution in the pore is different than for the WT pore. For the K163W mutant, we observed a single peak (12σ) in the pore, located between Lys^{159} and Arg^{155} (Fig. 5D), indicating that the mutant eliminates one of the anion binding sites.

Ion permeation and gating. Flux assays indicate that the pore of $Orai_{cryst}$ is closed, as would be expected before activation by STIM (Fig. 1). Because of the narrow width of the basic region of the pore and its extreme positive charge (Fig. 3B), we suspect that this section is not permeable to Ca^{2+} in its current conformation and forms a closed gate. Hydrophobic amino acids substituted for Lys^{163} (Arg^{91} in human Orai1), within the basic region, prevent channel activation (*40*). The structure of the K163W mutant indicates that the tryptophan residues make extensive hydrophobic interactions with each other and that the mutation eliminates one of the anion binding sites. Anion(s) bound in the basic region of a WT pore would probably occlude the pore and help stabilize the closed conformation. Whereas the hydrophobic packing in the mutants would probably be static, locking the channel in a closed conformation, an anion bound at Lys^{163} could dissociate, allowing the WT pore to open.

Table 1. Electron density in the basic region using different x-ray wavelengths. Peak heights of the F_o-F_c and anomalous-difference electron-density maps within the basic region are indicated for diffraction data sets from crystals (native unsoaked crystals from the same protein preparation and of comparable size and diffraction quality) that were collected at the indicated wavelengths. F_o-F_c maps were calculated using protein model phases (without ions in the pore) after rigid body refinement and with the resolution range 20 to 4 Å. Anomalous-difference electron-density maps were calculated using these phases and the resolution range 20 to 5 Å. Additional statistics are listed in table S3. The theoretical values for *f″* were obtained from the skuld.bmsc.washington.edu/scatter Web site.

Wavelength (Å)	Anomalous-difference peak height (σ)	Theoretical *f″* of iron (electrons)	F_o-F_c peak height (σ)
1.100	12.3	1.8	9.5
1.735	20.9	3.9	9.0
1.900	5.1	0.5	10.6

The structure suggests that the glutamate ring and hydrophobic section would be permeable to Ca^{2+} in the observed conformation. The distance between the oxygen atoms of the glutamate ring and the central axis of the pore is ~3 Å, which is similar to the typical coordination distance between Ca^{2+} and oxygen in crystal structures of Ca^{2+}-binding proteins (~2.4 Å) (*41*). This suggests that a Ca^{2+} ion would pass through the glutamate ring by coordinating the side chain oxygen atoms directly and becoming at least partially dehydrated. After emerging from the glutamate ring, the permeating Ca^{2+} ion would likely coordinate additional waters within the hydrophobic section. In support of this hypothesis, electron density consistent with water molecules is present within the hydrophobic section (fig. S5).

Experiments suggest that a cytosolic portion of STIM interacts with Orai to activate the channel (*24*, *42*–*44*) and that the interaction involves N- and C-terminal regions of Orai that correspond to the cytosolic region of M1 and the M4 extension in the structure (*23*, *24*, *27*–*29*, *45*). Deletion of the M4 extension or mutation of the residues that are observed to mediate its coiled-coil packing (Ile^{316} or Leu^{319}, corresponding to Leu^{273} and Leu^{276} in human Orai1) disrupts STIM binding and channel activation (*23*, *24*, *27*–*29*). This raises the possibility that STIM, which contains regions predicted to form coiled-coils, binds to the M4 extension by substituting for the coiled-coil interaction observed between the Orai subunits and that the arrangement of the M4 extensions in the structure is a quiescent one prior to the bind-

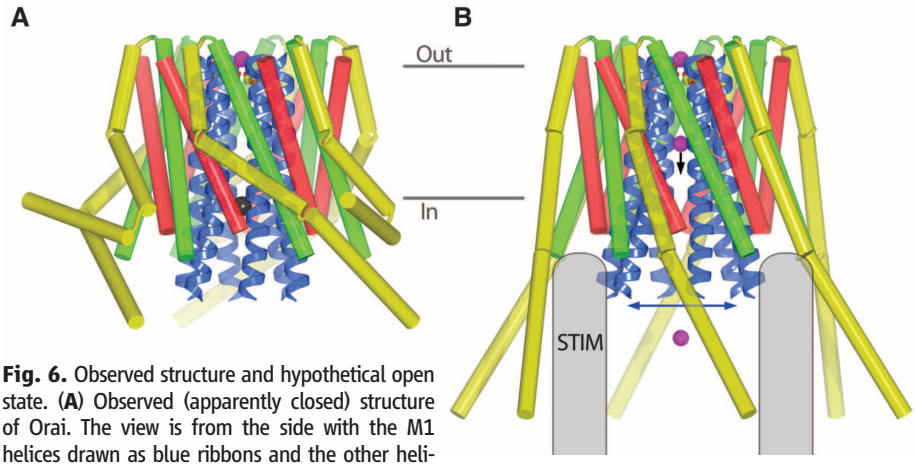

Fig. 6. Observed structure and hypothetical open state. (**A**) Observed (apparently closed) structure of Orai. The view is from the side with the M1 helices drawn as blue ribbons and the other helices shown as cylinders (M2, red; M3, green; M4 and M4 extension, yellow). A Ca^{2+} ion in the external site is depicted as a magenta sphere; an anion in the basic region of the pore is depicted as a gray sphere. Approximate boundaries of the lipid membrane are shown as horizontal lines. (**B**) Hypothetical model of an open state. The pore is widened by the outward dilation of the M1 helices (left-right arrow). A downward-pointing arrow indicates that Ca^{2+} is able to move though the pore unobstructed. The intracellular ends of the M1 helices are thought to interact with a cytosolic portion of STIM, as are the M4 extensions, which are modeled to protrude into the cytosol. The depiction of a cytosolic portion of STIM is meant to suggest that it might bridge the cytosolic portions of the M1 helices and the M4/M4 extension helices and is not meant to imply a particular structure, oligomeric state, or stoichiometry with Orai.

ing of STIM. Although C-terminal modifications of Orai disrupt STIM binding, deletion of the cytosolic portion of M1 or certain mutations within it (including the Orai1 mutants R91W and Lys^{85}, which faces away from the pore, to glutamate) have little effect on STIM binding but prevent channel activation (*23*, *24*, *45*). These observations are consistent with a hypothesis proposed by Park *et* al. that STIM binding provides the energy for channel gating by bridging the N- and C-termini of the channel (*24*).

Based on the structure and the available functional data, we constructed a working model for an open conformation of the channel (Fig. 6). In this model, the M4 extension helices project (>50 Å) into the cytosol and interact with a cytosolic portion of STIM. The basic region of the pore is dilated by the outward bending of the M1 helices (modeled to occur between Ser^{161} and Gly^{170}), which interact via their N-terminal regions with STIM. The M2-M3 loops (amino acids 220 to 235), while disordered in the current structure, might also make contributions, given their intracellular location and substantial conservation (fig. S1). Whether slight or dramatic, the dilation is expected to reduce the affinity of the basic region for anion(s), allowing them to be displaced.

Discussion. The crystal structure of Orai reveals an architecture that appears well suited to its physiological role. The ~10,000-fold resting concentration gradient of Ca^{2+} across the plasma membrane (~1 mM extracellular and ~100 nM intracellular Ca^{2+} concentrations) must be maintained to prevent aberrant Ca^{2+} signaling within cells; therefore, Orai must be tightly sealed shut when it is closed. Anion(s) bound in the basic region probably help serve this purpose. In an open conformation, the basic region would tend to prevent the permeation of cations that have modest concentration gradients (such as K^+ and Na^+, which have ~50-fold gradients) and, thus, would contribute to Ca^{2+}-selective permeation under physiological conditions. To establish a slow permeation rate that prevents overloading of the cell with Ca^{2+} and allows for fine tuning of sustained Ca^{2+} signals, the channel imposes energy barriers to ion permeation, which could include dissociation of Ca^{2+} from the selectivity filter (into the pore), permeation through the hydrophobic section, and electrostatic repulsion by the basic section. Ultimately, the channel's design takes advantage of the large Ca^{2+} gradient across the plasma membrane, while tightly regulating the flow of Ca^{2+} into the cell to mediate one of the most fundamental types of signaling in cell biology.

References and Notes

1. P. G. Hogan, R. S. Lewis, A. Rao, *Annu. Rev. Immunol.* **28**, 491 (2010).
2. J. Roos *et al.*, *J. Cell Biol.* **169**, 435 (2005).
3. S. L. Zhang *et al.*, *Nature* **437**, 902 (2005).
4. J. Liou *et al.*, *Curr. Biol.* **15**, 1235 (2005).
5. S. Feske *et al.*, *Nature* **441**, 179 (2006).
6. M. Vig *et al.*, *Science* **312**, 1220 (2006).
7. S. L. Zhang *et al.*, *Proc. Natl. Acad. Sci. U.S.A.* **103**, 9357 (2006).
8. A. V. Yeromin *et al.*, *Nature* **443**, 226 (2006).
9. M. Prakriya *et al.*, *Nature* **443**, 230 (2006).
10. M. Vig *et al.*, *Curr. Biol.* **16**, 2073 (2006).
11. Single-letter abbreviations for the amino acid residues are as follows: A, Ala; C, Cys; D, Asp; E, Glu; F, Phe; G, Gly; H, His; I, Ile; K, Lys; L, Leu; M, Met; N, Asn; P, Pro; Q, Gln; R, Arg; S, Ser; T, Thr; V, Val; W, Trp; and Y, Tyr.
12. S. Carrasco, T. Meyer, *Annu. Rev. Biochem.* **80**, 973 (2011).
13. B. A. McNally, M. Yamashita, A. Engh, M. Prakriya, *Proc. Natl. Acad. Sci. U.S.A.* **106**, 22516 (2009).
14. Y. Zhou, S. Ramachandran, M. Oh-Hora, A. Rao, P. G. Hogan, *Proc. Natl. Acad. Sci. U.S.A.* **107**, 4896 (2010).
15. A. Penna *et al.*, *Nature* **456**, 116 (2008).
16. W. Ji *et al.*, *Proc. Natl. Acad. Sci. U.S.A.* **105**, 13668 (2008).
17. O. Mignen, J. L. Thompson, T. J. Shuttleworth, *J. Physiol.* **586**, 419 (2008).
18. A. Demuro *et al.*, *Proc. Natl. Acad. Sci. U.S.A.* **108**, 17832 (2011).
19. M. Hoth, R. Penner, *J. Physiol.* **465**, 359 (1993).
20. A. Lepple-Wienhues, M. D. Cahalan, *Biophys. J.* **71**, 787 (1996).
21. C. Aussel, R. Marhaba, C. Pelassy, J. P. Breittmayer, *Biochem. J.* **313**, 909 (1996).
22. A. V. Yeromin, J. Roos, K. A. Stauderman, M. D. Cahalan, *J. Gen. Physiol.* **123**, 167 (2004).
23. Z. Li *et al.*, *J. Biol. Chem.* **282**, 29448 (2007).
24. C. Y. Park *et al.*, *Cell* **136**, 876 (2009).
25. Y. Zhou *et al.*, *Nat. Struct. Mol. Biol.* **17**, 112 (2010).
26. B. A. McNally, A. Somasundaram, M. Yamashita, M. Prakriya, *Nature* **482**, 241 (2012).
27. L. Navarro-Borelly *et al.*, *J. Physiol.* **586**, 5383 (2008).
28. M. Muik *et al.*, *J. Biol. Chem.* **283**, 8014 (2008).
29. I. Frischauf *et al.*, *J. Biol. Chem.* **284**, 21696 (2009).
30. D. A. Doyle *et al.*, *Science* **280**, 69 (1998).
31. Aspartate residues on the disordered M1-M2 loop (D182 and D184, corresponding to D110 and D112 in Orai1) probably also contribute to the acidic nature of the extracellular mouth of the pore.
32. S. L. Zhang *et al.*, *Proc. Natl. Acad. Sci. U.S.A.* **108**, 17838 (2011).
33. M. Hoth, *Pflugers Arch.* **430**, 315 (1995).
34. Y. Zhou, J. H. Morais-Cabral, A. Kaufman, R. MacKinnon, *Nature* **414**, 43 (2001).
35. A. Zweifach, R. S. Lewis, *Proc. Natl. Acad. Sci. U.S.A.* **90**, 6295 (1993).
36. M. Prakriya, R. S. Lewis, *J. Gen. Physiol.* **128**, 373 (2006).
37. B. Hille, in *Ionic Channels of Excitable Membranes* (Sinauer Associates, Sunderland, MA, ed. 2, 1992), pp. xiii.
38. D. Bakowski, A. B. Parekh, *Pflugers Arch.* **443**, 892 (2002).
39. B. D. James *et al.*, *Inorg. Chim. Acta* **247**, 169 (1996).
40. I. Derler *et al.*, *J. Biol. Chem.* **284**, 15903 (2009).
41. H. Kawasaki, R. H. Kretsinger, *Protein Profile* **2**, 297 (1995).
42. J. P. Yuan *et al.*, *Nat. Cell Biol.* **11**, 337 (2009).
43. M. Muik *et al.*, *J. Biol. Chem.* **284**, 8421 (2009).
44. T. Kawasaki, I. Lange, S. Feske, *Biochem. Biophys. Res. Commun.* **385**, 49 (2009).
45. A. Lis, S. Zierler, C. Peinelt, A. Fleig, R. Penner, *J. Gen. Physiol.* **136**, 673 (2010).

Acknowledgments: We thank J. Goldberg, M. B. Long, R. MacKinnon, and N. P. Pavletich for discussions and comments on the manuscript; C. D. Lima and members of the laboratory for discussions; E. Gouaux for green fluorescent protein fusion vectors; the staff of beamlines X25 and X29 (National Synchrotron Light Source, Brookhaven National Laboratory); the staff of the monoclonal antibody and proteomics and microchemistry facilities at MSKCC; the Keck Biophysics Resource at Yale University; and the Center for Applied Isotope Studies at the University of Georgia for protein analysis. This work was supported by the NIH (grant GM094273) and by a Burroughs Wellcome Career Award (to S.B.L). Atomic coordinates and structure factors have been deposited in the Protein Data Bank with accession numbers 4HKR (wild type) and 4HKS (K163W mutant).

Supplementary Materials

www.sciencemag.org/cgi/content/full/science.1228757/DC1
Materials and Methods
Supplementary Text
Figs. S1 to S6
Tables S1 to S3
References (*46*–*69*)

13 August 2012; accepted 16 October 2012
Published online 22 November 2012;
10.1126/science.1228757

www.sciencemag.org/cgi/content/full/science.1228757/DC1

Supplementary Materials for

Crystal Structure of the Calcium Release–Activated Calcium Channel Orai

Xiaowei Hou, Leanne Pedi, Melinda M. Diver, Stephen B. Long*

*To whom correspondence should be addressed. E-mail: longs@mskcc.org

Published 22 November 2012 on *Science* Express
DOI: 10.1126/science.1228757

This PDF file includes:

Supplementary Online Materials and Methods

Cloning, expression, purification, and crystallization. Orai from *Drosophila melanogaster* was selected for crystallization trials from among 53 Orai orthologs that were evaluated using a fluorescence-detection size-exclusion chromatography (FSEC) pre-crystallization screening technique (*46*) based on a sharp, symmetrical elution profile in several detergents. The protein construct used for structure determination contains residues 132-341 of *Drosophila melanogaster* Orai followed by a C-terminal antibody affinity tag that is recognized by the anti-tubulin antibody YL½ (*47*). The cDNA was cloned into the EcoRI and NotI restriction sites of the *Pichia pastoris* expression vector pPICZ-C (Invitrogen Life Technologies). It contains the following mutations: C224S and C283T (to prevent non-specific disulfide formation), and P276R and P277R (to produce well-ordered crystals). In this context, both the wild-type pore sequence ($Orai_{cryst}$) and the K163W pore mutant (K163W $Orai_{cryst}$) yielded crystals diffracting to 3.35 Å resolution. The complete amino acid sequence of $Orai_{cryst}$ is given (fig. S1). Transformation into *P. pastoris,* expression, and cell lysis were performed as previously described (*48*).

Lysed cells were re-suspended in buffer (6 ml buffer for each 1 g of cells) containing 150 mM KCl, 10 mM sodium phosphate, pH 7.0, 0.1 mg/ml deoxyribonuclease I (Sigma-Aldrich), 1:1000 dilution of Protease Inhibitor Cocktail Set III, EDTA free (CalBiochem), 1 mM benzamidine (Sigma-Aldrich), 0.5 mM 4-(2-Aminoethyl) benzenesulfonyl fluoride hydrochloride (Gold Biotechnology) and 0.1 mg/ml soybean trypsin inhibitor (Sigma-Aldrich). Cell lysate was adjusted to pH 7.0 with 1 N KOH, 0.11 g n-dodecyl-β-D-maltopyranoside (DDM, Anatrace, solgrade) per 1 g of cells was added to the cell lysate, and the mixture was stirred at room temperature for 45 minutes to extract Orai from the membranes. The sample was then centrifuged at 40,000 *g* for 45 min at 12°C and the supernatant was filtered (0.45 μm polyethersulfone membrane). YL½ antibody (IgG, expressed from hybridoma cells and purified by ion exchange chromatography using standard methods) was coupled to CNBr-Activated Sepharose beads (GE Healthcare) according to the manufacturer's protocol. Approximately 0.4 ml of beads were added to the sample for each 1 g of *P. pastoris* cells and the mixture was rotated at room temperature for 1 h. Beads were collected on a column, washed with 5 column-volumes of buffer containing 150 mM KCl, 10 mM sodium phosphate, pH 7.0, 5 mM DDM, 0.1 mg/ml lipids (3:1:1 weight ratio of 1-Palmitoyl-2-Oleoyl-sn-

Glycero-3-Phosphocholine, 1-Palmitoyl-2-Oleoyl-sn-Glycero-3-Phosphoethanolamine, and 1-Palmitoyl-2-Oleoyl-sn-Glycero-3-[Phospho-rac-(1-glcerol)], obtained from Avanti) and eluted with buffer containing 150 mM KCl, 100 mM Tris-HCl, pH 8.5, 5 mM DDM, 0.1 mg/ml lipids and 5 mM Asp-Phe peptide (Sigma-Aldrich). The eluted protein was concentrated to ~ 25 mg/ml using a 100 kDa concentrator (Amicon Ultra, Millipore) and further purified on a Superdex-200 gel filtration column (GE Healthcare) in 75 mM KCl, 10 mM Tris-HCl, pH 8.5, 0.1 mg/ml lipids, 8 mM n-Nonyl-β-D-maltopyranoside (NM, Anatrace, anagrade), and 8 mM n-Nonyl-β-D-glucopyranoside (NG, Anatrace, anagrade). The fraction corresponding to Orai was concentrated to ~ 16 mg/ml using a 100 kDa Vivaspin-2 concentrator (Sartorius Stedim Biotech), mixed 1:1 with crystallization solution and set up as hanging drops over reservoirs containing 0.5 ml of well solution. Crystals grew in 24-29% polyethylene glycol 400 (v/v), 1 M ammonium formate, 100 mM MES, pH 5.6-6.5 at 17°C and reached ~ 150 μm size within two weeks. The same methods were used for expression, purification and crystallization of the K163W mutant.

Structure determination. Crystals were cryo-protected by placing them into a stabilization solution containing the buffer components of an equilibrated crystallization drop and the PEG 400 concentration was increased from 30% to 50% (v/v) in a step-wise manner (2.5% increase each step, 1 minute intervals). The crystals were then flash-cooled in liquid nitrogen. Derivatives and crystals soaked in metals were prepared in the following ways. For crystals with Ba^{2+} or Ca^{2+} the crystals were incubated in stabilization solution supplemented with 50 mM $BaCl_2$ or 50 mM $CaCl_2$ for 5 h and then transferred into cryo-protection solution supplemented with these salts and then flash-cooled. For other complexes, crystals were soaked in stabilization solution supplemented with ~18 μg/ml p-chloromercuribenzene sulfate (PCMB), 1 mM $GdCl_3$, or 2 mM Na_3IrCl_6 (Hampton Research). After soaking in PCMB (8 hours), $GdCl_3$ (48 hours) or Na_3IrCl_6 (48 hours), the crystals were cryo-protected in the same solutions as native crystals and flash-cooled. A crystal of K163W $Orai_{cryst}$ soaked in 50 mM $CaCl_2$ and a crystal of $Orai_{cryst}$ soaked in 50 mM $BaCl_2$ gave the best X-ray diffraction (each to 3.35 Å resolution) and these datasets were used for structure determination. Diffraction data were processed with the HKL suite (*49*). Highly redundant datasets, due in part to the high symmetry of the space group, were obtained by using short X-ray exposures (0.5 - 1 second

per degree at NSLS beamline X25) in order to minimize radiation decay and by merging oscillation images from 180-500 degrees of crystal rotation. The number of oscillation images merged for each dataset was chosen based on the I/σ(I) and B factor values (as reported in HKL-2000) and from inspection of electron density maps. The final datasets were generated by including oscillation images beginning with the first image until the image where the B factor reached ~10 (this gave the highest I/σ(I) in the outer resolution range and yielded electron density maps with well-defined features).

Initial phases (35-6.0 Å) were determined using crystals of K163W $Orai_{cryst}$ by the MIRAS method from a native dataset and three derivative ones (PCMB, $GdCl_3$, and Na_3IrCl_6) using autoSHARP and SHARP (*50*) (Table S1). The phases were improved and extended to 3.35 Å resolution using solvent flattening, histogram matching, and twofold non-crystallographic symmetry (NCS) averaging with the program DM (*51*), and yielded electron density maps with well-defined features (fig. S2). The model of K163W $Orai_{cryst}$ was built using O (*52*) and COOT (*53*), and refined with CNS (*54*) and PHENIX (version 1.8.1) (*55*) using NCS restraints. Both the structure factor amplitudes and the experimental phases were used during refinement because this yielded a lower R_{free} value and reduced the separation between the R_{free} and R_{work} values in comparison to refinement strategies that used only the structure factor amplitudes. Initial phases for the structure of $Orai_{cryst}$ were determined by rigid body refinement using the K163W $Orai_{cryst}$ coordinates (with the side chain of amino acid 163 removed). Potential phase bias was minimized by using the anomalous signals present in the dataset (subsequently determined to be due to zinc, iron, and barium sites) for MR-SAD phasing in PHENIX (*55*) and by density modification using DM (*51*) (fig. S2). Adjustments to the model of $Orai_{cryst}$ were made with O (*52*) and COOT (*53*), and it was refined with CNS (*54*) and PHENIX (*55*) using NCS restraints. Both final models ($Orai_{cryst}$ and K163W $Orai_{cryst}$) contain residues 144-334 of Orai, excluding the following residues that did not have well-enough defined electron density to direct model building: 330-334 of subunit B, 181-190 (the M1-M2 loop) and 220-235 (the M2-M3 loop). Because the M1-M2 and M2-M3 loops are disordered, there is some ambiguity with regard to which subunit each of the M1 and M2 helices belongs to. In the atomic model, the subunits (chain identifiers) are assigned so as to have the

shortest atomic distances for the M1-M2 and M2-M3 loops. Some side chains on the solvent-exposed surfaces of the channel are truncated in the model because the electron density was not sufficient for placement. Figures were prepared using the program PyMOL (www.pymol.org); the programs HOLE (*56*) (Fig. 3B) and APBS (*57*) (Figs. 3C & D) were also utilized (with default parameters).

Reconstitution into vesicles and flux assay. Three Orai constructs ($Orai_{cryst}$, K163W $Orai_{cryst}$, and V174A $Orai_{cryst}$) were purified and reconstituted into lipid vesicles (at the same time) using a published procedure (*58*) with modifications. A POPE (1-palmitoyl-2-oleoyl-sn-glycero-3-phosphocholine) and POPG (1-palmitoyl-2-oleoyl-sn-glycero-3-phospho-(1'-rac-glycerol)) lipid mixture (15 mg/ml:5 mg/ml) was prepared and solubilized with 8% n-Octyl-β-D-maltopyranoside (OM). The proteins were then mixed (1:1) with the solubilized lipids to give a final protein concentration of 0.1 mg/ml (1:100 protein:lipid ratio). Detergent was removed by dialysis (8000 Da molecular weight cutoff) at 4°C for 5 days against a reconstitution buffer containing 10 mM HEPES, pH 7.0, 150 mM NaCl and 0.2 mM ethylene glycol tetraacetic acid (EGTA). The resulting protein/lipid vesicles were sonicated (~30 sec), divided into small aliquots, flash-frozen in liquid nitrogen, and stored at -80 °C. The empty vesicles were prepared in the same manner without adding protein prior to dialysis.

The flux assay was adapted from other such assays (*59-62*). Briefly, vesicles were thawed, sonicated for 5 sec and diluted by 100-fold into a flux assay buffer (FAB) consisting of 150 mM n-methyl-d-glucamine (NMDG), 10 mM HEPES, pH 7.0, 0.2 mM EGTA, 0.5 mg/ml bovine serum albumin, and 2 μM 9-amino-6-chloro-2-methoxyacridine (ACMA, Sigma-Aldrich, from a 2 mM stock in DMSO). Data were collected on a SpectraMax M5 fluorometer (Molecular Devices) using the Softmax Pro 5 software package. Fluorescence intensity measurements were collected every 30 sec (for a total of 1200 or 1500 sec) with excitation and emission set to 410nm and 490nm, respectively. The proton ionophore carbonyl cyanide m-chlorophenyl hydrazone (CCCP, Sigma-Aldrich; 1 μM from a 1 mM stock in DMSO) was added after 150 seconds and the sample was gently mixed with a pipette. Monensin (Sigma-Aldrich; 20 nM final concentration from a 20 μM stock in DMSO) was added at 990 seconds to release Na^+ from all the vesicles. For Gd^{3+} blockage

experiments, 0.3 mM $GdCl_3$ was added to the vesicles before sonication and to the FAB, and the assay was performed as described above.

Cross-linking and light scattering. For crosslinking in membranes, cDNA for *Drosophila melanogaster* Orai (amino acids 119-351; wild-type sequence; with a stop codon following amino acid 351) was cloned into the expression vector pCGFP-EU (*46*), transfected into HEK293 cells (Invitrogen) using Lipofectamine 2000 (Invitrogen), and the cells were cultured for 48 h. Cells were harvested and re-suspended in a buffer consisting of 150 mM KCl, 50 mM sodium phosphate, pH 8.0, and 1:500 dilution of Protease Inhibitor Cocktail Set III, EDTA-free (CalBiochem) and lysed by dounce homogenization and brief sonication (30 sec) in a bath sonicator. Cell debris was removed by centrifugation (2500 *g*, 4°C, 10 min) and the membrane fraction was collected by ultracentrifugation (100,000 *g*, 4°C, 1 h) and then re-suspended in the same buffer (using a Dounce homogenizer followed by a 10 sec sonication). The membranes were then treated with disuccinimidyl suberate crosslinker (Pierce, 0 – 250 μM) for 30 min at room temperature. The reactions were stopped by the addition of 70 mM Tris-HCl, pH 8.5, run on a 4-15 % SDS-polyacrylamide gel under reducing conditions (100 mM dithiothreitol), and detected by Western blot using an antibody raised against purified *Drosophila melanogaster* Orai in mice.

For crosslinking of purified protein, purified Orai (amino acids 119-351 with the wild-type sequence and followed by a YL½ affinity tag) was exchanged by gel filtration into buffer consisting of 150 mM NaCl, 20 mM sodium phosphate, pH 7.5, and 1 mM DDM. The protein was concentrated to 1.0 mg/ml, and treated with disuccinimidyl suberate crosslinker (Pierce, 0 – 700 μM) for 30 min at room temperature. The reactions were stopped by adding 70 mM Tris-HCl, pH 8.5, and analyzed by 4-15% SDS-polyacrylamide gel electrophoresis under reducing conditions (100 mM dithiothreitol).

The SEC-LS/RI/UV (size-exclusion chromatography coupled with "on-line" static laser light scattering, refractive index, and ultraviolet absorption) experiments were carried out by the Keck Biophysics Resource at Yale University (fig. S3A). Purified Orai (residues 132-341, containing the K163W mutation, and followed by a YL½ affinity tag; at 1.4 mg/ml in SEC buffer: 150 mM NaCl, 20 mM Tris-HCl, pH 8.5, and 1 mM DDM) was injected, using an autosampler, onto a Superose 6, 10/30, HR Size Exclusion Chromatography (SEC) column (GE Healthcare) that

was connected to a High Performance Liquid Chromatography System (Agilent 1200; Agilent Technologies). The elution from the SEC column was monitored by a photodiode array (PDA) UV/VIS detector (Agilent Technologies), a differential refractometer (OPTI-Lab rEx Wyatt Corp.), and a multiangle laser light scattering (LS) detector (HELEOS II with QELS capability, Wyatt Corp.). The SEC-UV/LS/RI system was equilibrated in SEC buffer and run at a flow rate of 0.3 ml/min. Two software packages were used for data collection and analysis: the Chemstation software (Agilent Technologies) controlled the HPLC operation and data collection from the multi-wavelength UV/VIS detector, while the ASTRA software (Wyatt Corp.) collected data from the refractive index detector, the light scattering detectors, and recorded the UV trace at 280 nm sent from the PDA detector. The polypeptide component of the total molecular weight (polypeptide+lipids+detergent) was determined as previously described (*63-65*). The weight-average molecular masses were determined across the entire elution profile in 1 sec intervals from static LS measurements using ASTRA software as previously described (*66*).

	K163W $Orai_{cryst}$				$Orai_{cryst}$			
	Native Ca^{2+}	**Derivative 1** PCMB	**Derivative 2** Gd^{3+}	**Derivative 3** $(IrCl_6)^{3-}$	**Ba^{2+}**	**Ca^{2+}**	**Gd^{3+}**	**$(IrCl_6)^{3-}$**
Datasets source	NSLS X29	NSLS X25	NSLS X25	NSLS X25	NSLS X25	NSLS X25	NSLS X25	NSLS X25
Wavelength (Å)	1.0750	0.9900	1.7000	1.1041	1.1000	1.1000	1.7000	1.1033
Cell dimensions:								
a= b= c (Å)	118.309	118.401	118.250	118.072	117.910	117.816	119.028	118.522
α= β= γ (°)	90	90	90	90	90	90	90	90
Resolution (Å)	45-3.35 (3.41-3.35)	50-3.90 (3.97-3.90)	50-4.20 (4.27-4.20)	50-4.20 (4.27-4.20)	40-3.35 (3.41-3.35)	40-3.80 (3.87-3.80)	50-4.50 (4.58-4.50)	45-3.65 (3.71-3.65)
No. of crystals	1	1	1	1	1	1	1	1
R_{sym} (%)	8.3 (>100)	10.6 (>100)	6.9 (>100)	8.5 (>100)	7.2 (>100)	6.5 (>100)	8.1 (>100)	6.7 (>100)
I/σI	35.3 (1.3)	42.4 (1.3)	59.8 (1.4)	58.2 (1.4)	59.7 (1.2)	65.3 (1.3)	37.3 (1.1)	68.5 (1.3)
Completeness (%)	99.7 (100.0)	100.0 (100.0)	100 (100)	100 (100)	100 (100)	100 (100)	100 (100)	100 (100)
Redundancy	24.3 (23.4)	41.4 (43.0)	30.1 (29.4)	35.9 (37.8)	40.5 (40.7)	38.0 (38.9)	30.0 (28.8)	36.0 (33.9)
MIRAS Phasing								
No. of sites		3†	1	2†				
Phasing power (iso/ano)		1.016 / 1.777	0.351 / 0.709	0.259 / 0.807				
R_{cullis} (iso/ano)		0.812 / 0.619	0.895 / 0.898	0.978 / 0.864				
Figure of Merit (SHARP)	0.582 [35-6.0Å]							
Figure of Merit (DM)	0.761 [35-3.35Å]							
Refinement	K163W $Orai_{cryst}$ final coordinates			Rigid body¶	$Orai_{cryst}$ final coordinates	Rigid body‡	Rigid body‡	Rigid body‡
Resolution (Å)	20-3.35			20-4.20	20-3.35	20-3.80	20-4.50	20-3.65
No. of reflections	8081			4110	7995	5496	3333	6222
No. atoms	2358			2356	2353	2349	2349	2349
R_{work} (%)	27.9			29.6	27.8	28.5	30.9	29.3
R_{free} (%)	28.3			29.8	27.9	27.4	29.6	29.4
Ramachandran (%)								
Favored	97				97			
Outliers	0				0			
R.m.s.d:								
bond lengths (Å)	0.011				0.009			
bond angles (°)	1.47				1.34			

Table S1. Data collection, phasing and refinement statistics. Data collection statistics are from HKL2000. $R_{sym} = \Sigma \mid I_i - < I_i > \mid / \Sigma I_i$, where $< I_i >$ is the average intensity of symmetry-equivalent reflections. Phasing power = RMS ($|F|/\varepsilon$), where $|F|$ is the heavy-atom structure factor amplitude and ε is the residual lack of closure error. R_{cullis} is the mean residual lack of closure error divided by the dispersive or anomalous difference. R-factor $= \Sigma \mid F_o - F_c \mid / \Sigma \mid F_o \mid$, where F_o and F_c are the observed and calculated structure factors, respectively. R_{free} = R-factor calculated using a subset (~5%) of reflection data chosen randomly and omitted throughout refinement. The figure of merit is indicated from MIRAS analysis (using SHARP) and after density modification and phase extension (using DM). †One of these sites was later identified as a zinc ion in a crystal contact (fig. S6). R.m.s.d : root mean square deviations from ideal geometry. Numbers in parentheses indicate the highest resolution shells and their statistics. ¶Rigid body refinement using the final model of K163W $Orai_{cryst}$ with the ions removed. ‡Rigid body refinement using the final model of $Orai_{cryst}$ with the ions removed.

	$Orai_{cryst}$		K163W $Orai_{cryst}$	
	Buffer (ppb)	**Protein** (ppb)	**Buffer** (ppb)	**Protein** (ppb)
Cr	8	11	14	19
Mn	2	15	0	4
Fe	**0**	**2995 (54 μM)**	**4**	**999 (18 μM)**
Co	0	3	0	4
Ni	4	21	6	26
Cu	49	66	23	71
Zn	**3**	**712 (10 μM)**	**10**	**711 (10 μM)**
As	2	4	4	4
Sr	0	3	0	0
Ag	0	0	1	1
Cd	0	0	1	1
Ba	2	17	1	4
Au	0	0	0	0
Pb	1	3	1	2

Table S2. ICP-MS analysis. Purified protein at ~ 80 μM (~ 13 μM hexamer concentration) was analyzed by inductively coupled plasma - mass spectrometry (ICP-MS) by the Center for Applied Isotope Studies at the University of Georgia. The amounts (in parts per billion, ppb) of various metals in samples of $Orai_{cryst}$, K163W $Orai_{cryst}$, or the buffers used for purification are listed; the corresponding molar concentrations for zinc and iron are also indicated.

	$Orai_{cryst}$		
x-ray source	NSLS X25	NSLS X25	NSLS X25
Wavelength (Å)	1.100	1.735	1.900
Cell dimensions:			
a= b= c (Å)	117.647	117.799	117.785
α= β= γ (°)	90	90	90
Resolution (Å)	50-3.80 (3.87-3.80)	50-3.90 (3.97-3.90)	50-3.90 (3.97-3.90)
No. of crystals	1	1	1
R_{sym} (%)	5.3 (>100)	5.5 (>100)	6.9 (>100)
I/σI	81.9 (1.2)	81.1 (1.4)	64.0 (1.5)
Completeness (%)	100 (100)	100 (100)	100 (100)
Anomalous redundancy	38.8 (39.8)	38.0 (37.9)	37.1 (36.8)
Refinement (rigid body)			
Resolution (Å)	20-3.8	20-3.9	20-3.9
R_{work} (%)	31.1	31.2	32.0
R_{free} (%)	31.7	32.1	32.5
F_o-F_c peak height in basic region of pore (σ)	9.5	9.0	10.6
Theoretical *f'* of iron (electrons)	0.1	-5.0	-2.2
Anomalous difference peak height in basic region of pore (σ)	12.3	20.9	5.1
Theoretical *f"* of iron (electrons)	1.8	3.9	0.5

Table S3. Expanded version of Table 1, showing data collection and refinement statistics for datasets from $Orai_{cryst}$ crystals (un-soaked native crystals) that were collected at different x-ray wavelengths. Data collection statistics are from HKL2000. $R_{sym} = \Sigma \mid I_i - < I_i > \mid / \Sigma I_i$, where $< I_i >$ is the average intensity of symmetry-equivalent reflections. R-factor = $\Sigma \mid F_o - F_c \mid / \Sigma \mid F_o \mid$, where F_o and F_c are the observed and calculated structure factors, respectively. R_{free} = R-factor calculated using a subset (~5%) of reflection data chosen randomly and omitted throughout refinement. The peak heights of the F_o-F_c and anomalous difference electron densities in the basic region of the pore are indicated. F_o-F_c maps (20 - 4 Å resolution) were calculated using protein model phases (without ions in the pore) after rigid body refinement (using the final model of $Orai_{cryst}$ with the ions removed). Anomalous difference electron density maps were calculated using these phases and the resolution range 20 – 5 Å. The theoretical values for *f'* and *f"* (where the x-ray scattering factor $f = f_o + f' + if"$, and f_o is the normal atomic scattering factor, *f'* is the real component of the anomalous scattering factor, and *f"* is the imaginary component of the anomalous scattering factor) were obtained from the skuld.bmsc.washington.edu/scatter Web site.

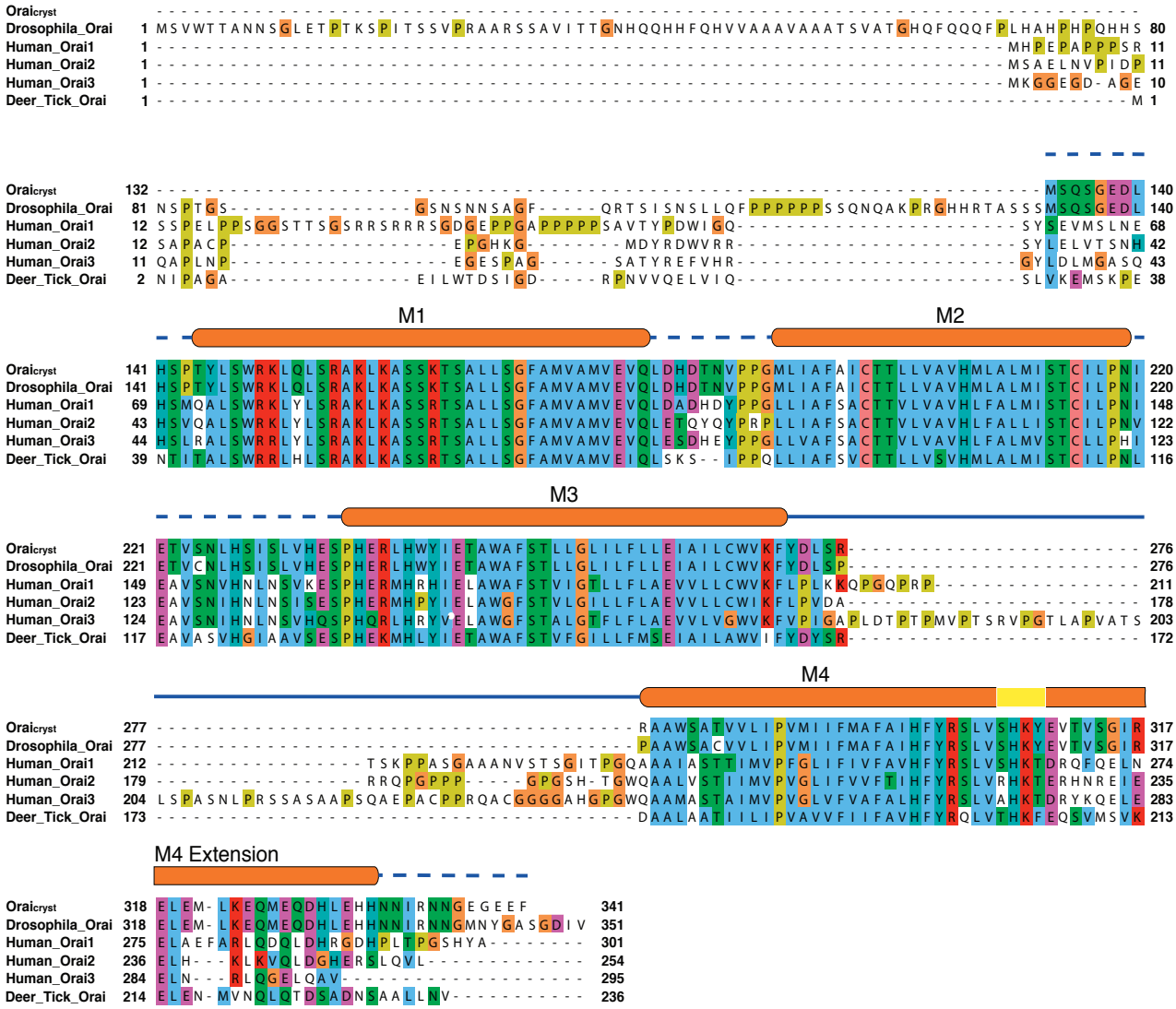

fig. S1. Sequence alignment. The complete amino acid sequence of the crystallized construct is given ($Orai_{cryst}$). The secondary structure is indicated above the alignment, with dashed regions denoting portions that are disordered and cylinders representing α helices. The yellow colored region denotes the bend between M4 and the M4 extension. The sequence of the M3-M4 loop in deer tick Orai served as a basis for design of mutations in the M3-M4 loop that yielded well-diffracting crystals. The accession numbers for the sequences in the alignment below $Orai_{cryst}$ are: Q9U6B8, Q96D31, Q96SN7, Q9BRQ5, and B7PLW7.

A

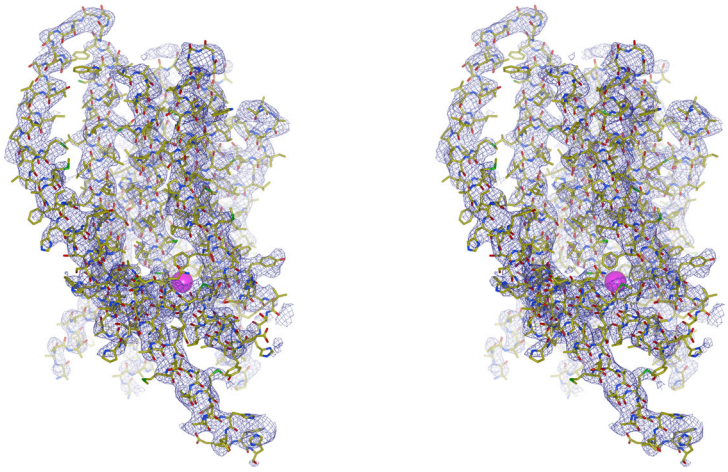

B

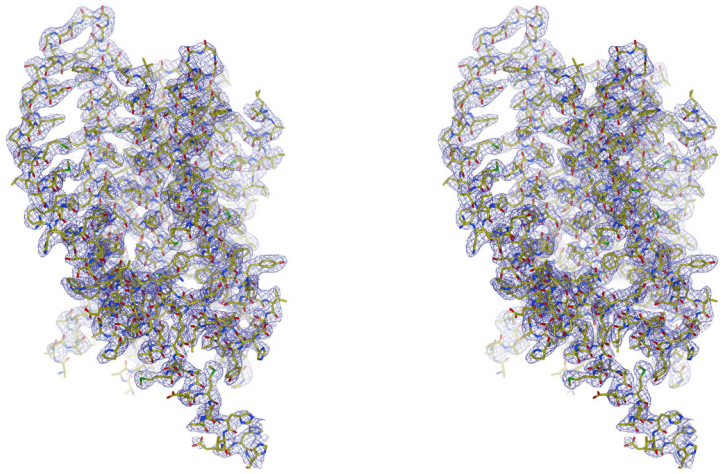

C

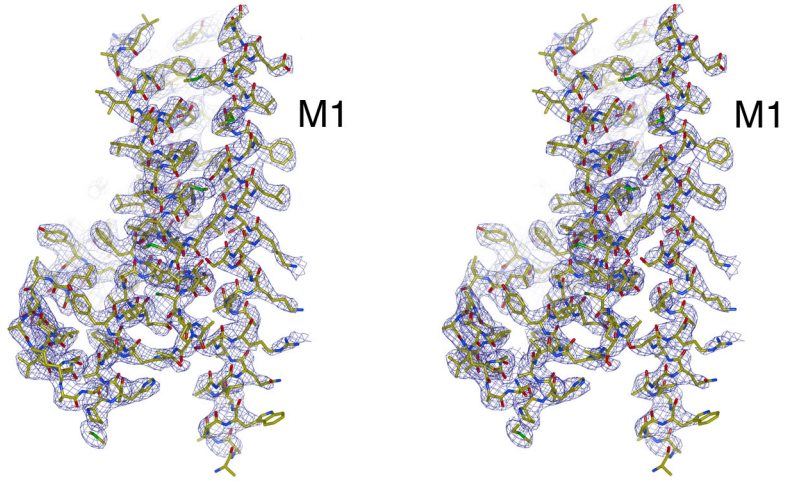

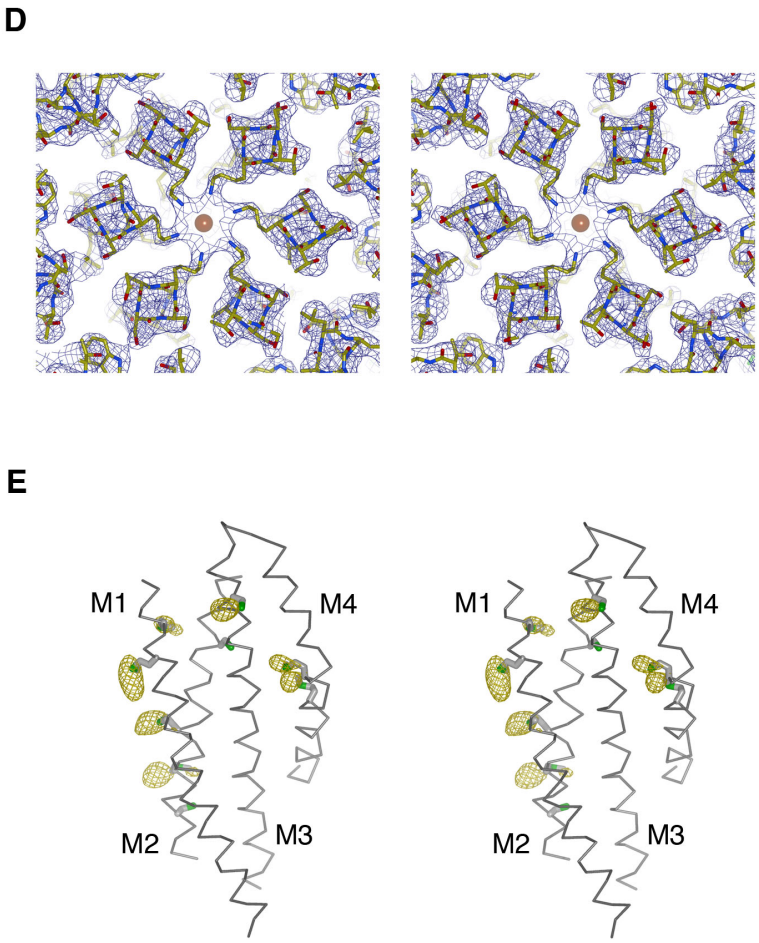

fig. S2. Electron density maps, shown in stereo. (**A**) The experimental electron density map for K163W $Orai_{cryst}$ (blue mesh) contoured at 1.3σ and covering the final model (stick representation, showing subunits A and B). The map was calculated from 35 - 3.35 Å resolution using native-sharpened amplitudes and MIRAS phases after solvent flattening, histogram matching, and NCS averaging. Magenta spheres represent the location of mercury atoms (from the PCMB derivative) adjacent to Cys 215. The view is of two complete subunits within the asymmetric unit from the side, with the extracellular solution above. (**B**) The electron density map for $Orai_{cryst}$. The map was calculated from 35 – 3.35 Å resolution using native-sharpened amplitudes and MR-SAD phases (K163W $Orai_{cryst}$ molecular replacement phases combined with phases derived from the anomalous difference diffraction signal in the $Orai_{cryst}$ dataset) after solvent flattening, histogram matching, and NCS averaging. The map is contoured at 1.3σ and the orientation is the same as in (A). (**C**) Close up view of a portion of the electron density from (B), covering the transmembrane region of subunit A. The M1 helix is indicated and the view is from the side with the extracellular solution above. (**D**) Close up view of a portion of the density from (B), showing the density for Lys 163. The view is from the extracellular side, within the pore, and all six subunits are drawn. The density ascribed to iron (brown sphere) is at the center. (**E**) Anomalous-difference electron-density (yellow mesh) for sulfur atoms of cysteine and methionine residues. The map was calculated from data collected with λ=1.90 Å x-rays, using phases from the protein model (20 – 5 Å resolution and contoured at 3 σ). The transmembrane region of subunit A is shown as a wire representation (Cα trace) with the cysteine and methionine residues drawn as sticks.

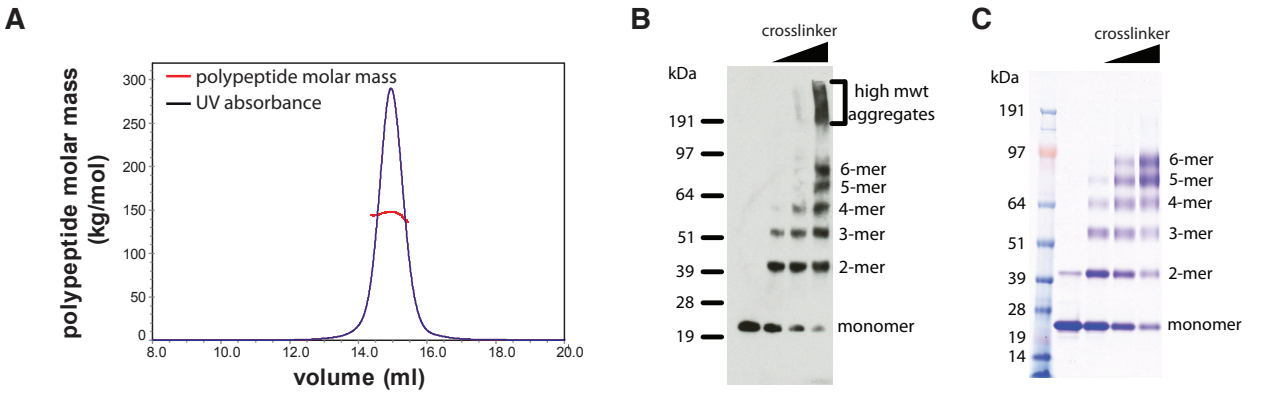

fig. S3. Subunit stoichiometry and molecular mass determination from crosslinking and light scattering experiments. (**A**) Molecular mass determination of purified Orai from SEC-LS/RI/UV measurements. The elution profile (UV trace, black) of Orai from size-exclusion chromatography (SEC) is shown. Analysis of the monodisperse peak of Orai according to (*63-65*) indicated a polypeptide molecular mass of 149 ± 6 kDa (red trace), indicating an oligomeric state of 6.1 ± 0.2 subunits. (Based on the amino acid sequence, the theoretical mass of one subunit is 24.28 kDa.) The molecular mass of the polypeptide+detergent+lipid complex was determined to be 257 ± 6 kDa from the SEC-LS/RI/UV measurements. The elution volumes for the water-soluble protein standards that were used for calibration are: carbonic anhydrase (29.0 kDa) at 18.24 ml, ovalbumin (43.2 kDa) at 17.36 ml, bovine serum albumin (66.3 kDa) at 16.55 ml, aldolase (156 kDa) at 16.03 ml, and beta-amylase (220 kDa) at 15.34 ml. The elution volume for Orai is 14.95 ml. (**B**) Crosslinking of Orai in HEK293 cell membranes. Increasing amounts of crosslinker (0, 25, 75, 250 μM disuccinimidyl suberate) were used and Orai was detected by western blot using a monoclonal antibody. The positions of molecular weight standards are indicated. (**C**) Crosslinking of purified Orai in detergent. Increasing amounts of crosslinker (0, 70, 200, 700 μM disuccinimidyl suberate) were used and Orai was analyzed by SDS-PAGE and detected by coomassie stain. Molecular weight standards are located in the first lane. The purified protein contains an affinity tag, which increases its molecular weight slightly relative to (B).

Supplementary discussion. The SEC-LS/RI/UV technique (size-exclusion chromatography coupled with "on-line" static laser light scattering, refractive index, and ultraviolet absorption technique) allows the molecular mass of purified membrane proteins to be determined (*63-65*). Using this technique, which can distinguish between the polypeptide and the detergent/lipid components of the total molecular mass, the oligomeric state of purified Orai was determined to be 6.1 ± 0.2 subunits (fig. S3A). Crosslinking of Orai in cell membranes and crosslinking of purified Orai in detergent were consistent with a hexameric assembly (figs. S3B and C). The crosslinking reagent (disuccinimidyl suberate, which has a spacer of ~ 11 Å between its amine-reactive groups) did not cause a full shift to the hexameric gel mobility, possibly because of the limited number of lysine residues available on Orai for reaction with it. Similar results were observed using glutaraldehyde and disuccinimidyl glutarate crosslinking reagents.

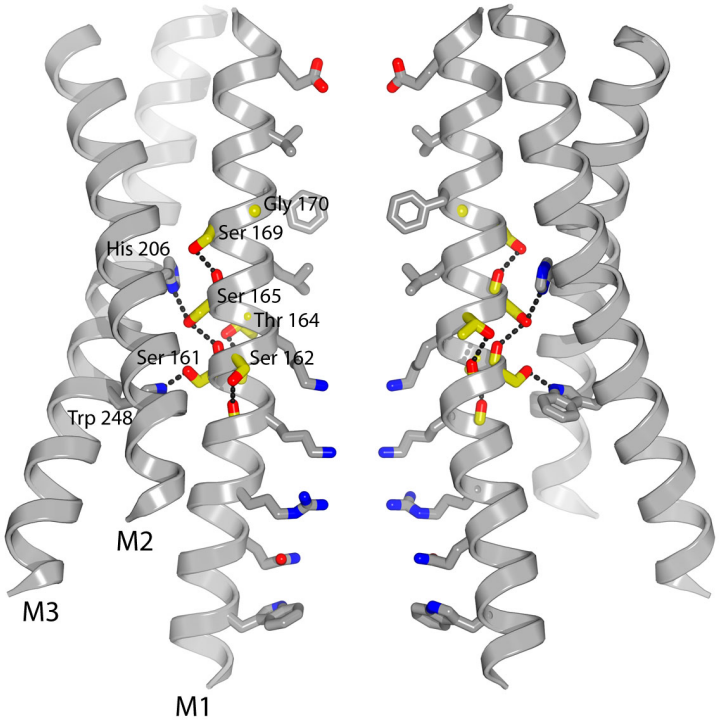

fig. S4. Serine, threonine and glycine residues on M1. M1-M3 helices (grey ribbons) from two subunits are shown (four subunits are omitted) with serine, threonine and glycine residues on M1 drawn as yellow (carbon) and red (oxygen) sticks. Pore-lining residues on M1 are drawn as sticks (grey colored carbon atoms). Probable hydrogen bonds between serine/threonine side chain hydroxyls and backbone carbonyl oxygen atoms (red) are shown as dotted lines. Possible hydrogen bonds to the side chains of His 206 and Trp 248 are also shown.

Supplementary discussion. Amino acids that are sometimes associated with bends in α-helices (serine, threonine, and glycine) (*67*) are highly represented in the portion of M1 that spans the inner leaflet of the membrane (Ser 161, Ser 162, Thr 164, Ser 165, Ser 169 and Gly 170) (fig. S4). Although the resolution limit of the diffraction data limits the certainty of hydrogen bond interactions, a slight bend in M1 at Ser 162 seems to involve a typical arrangement (*67*) in which a serine (or threonine) side chain hydroxyl forms a hydrogen bond with the backbone carbonyl oxygen of a residue of the preceding helical turn (Leu 158) (fig. S4). Thr 164, Ser 165 and Ser 169 also appear to form hydrogen bonds with backbone carbonyl oxygen atoms (of Ala 160, Ser 161 and Ser 165, respectively). While M1 does not bend at these positions in the current structure, these hydrogen bonds make it appear that it is poised to do so. The side chain hydroxyls of Ser 165 and Ser 161 probably form hydrogen bonds with His 206 and Trp 248 on M2 and M3 (His 206 ND1 atom and Trp 248 NE1 atom, respectively). Glycine residues can also allow transmembrane helices to bend, as has been observed in K^+ channels where a glycine residue serves as a 'gating hinge' that permits conformational change within the helices that line the pore (*68, 69*). Gly 170 (Gly 98 in human Orai1) has been proposed to serve a similar function in Orai (*32*).

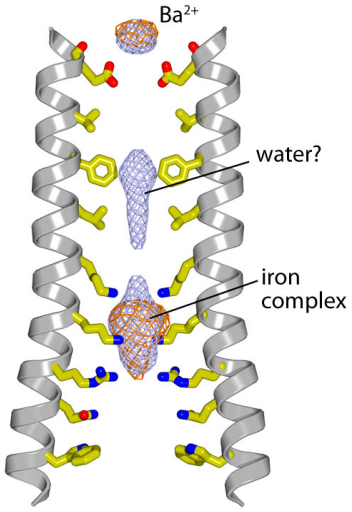

fig. S5. Electron density in the pore of $Orai_{cryst}$. A simulated annealing omit F_o-F_c electron density map (blue mesh) and an anomalous difference density map (orange mesh) are shown within the pore. The diffraction data used for the maps are from the crystal of $Orai_{cryst}$ containing $BaCl_2$ that was used for refinement (Table S1). The F_o-F_c map was calculated using model phases after simulated annealing refinement with atoms in the pore omitted (4σ contour, 20 – 3.35 Å resolution). The anomalous difference map was calculated using these phases (4σ contour, 20 – 5 Å resolution).

Supplementary discussion. Some unidentified electron density is present within the hydrophobic section of the pore (adjacent to Phe 171 and Leu 167, fig. S5). Because anomalous difference density was not observed there, it may be due to water molecules.

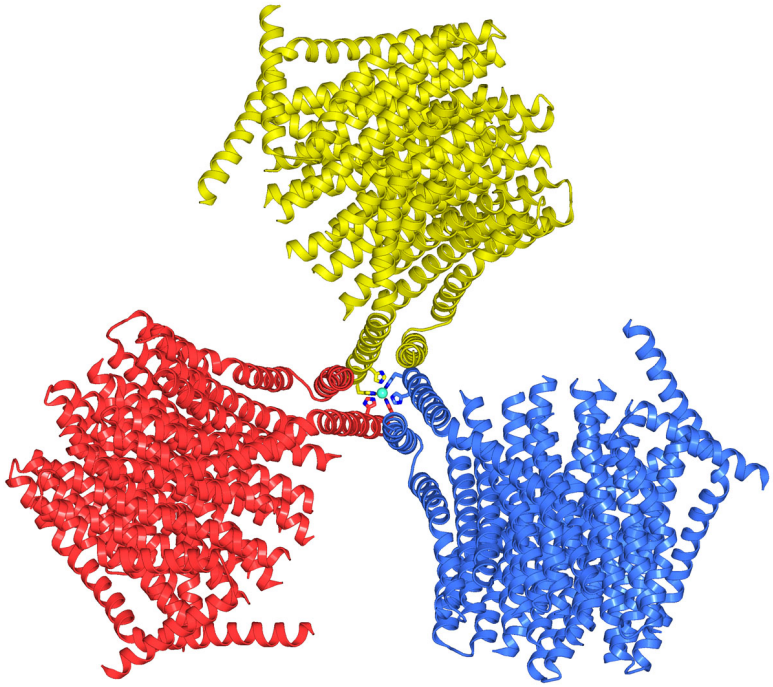

fig. S6. Crystal packing. Three channel hexamers are shown in ribbon representation (blue, red and yellow) around the only ordered crystal contact between channels in the crystal. The crystal contact involves two histidine residues (His 330 and His 334, drawn as sticks) on the M4 extension of subunit A that coordinate a zinc ion (teal sphere) at the center of a threefold crystallographic symmetry axis. The ion was identified as zinc from ICP-MS analysis and from peak heights at the site in anomalous-difference electron-density maps that were calculated from datasets collected using x-ray wavelengths above and below an absorption edge of zinc (λ=1.284 Å). Using λ=1.281 Å x-rays, where the *f*" of zinc is approximately 3.9 electrons, gave a peak height of ~ 10σ. Using λ=1.300 Å x-rays, where the *f*" of zinc is approximately 0.5 electrons, gave a peak height of less than 3σ.

References and Notes

1. P. G. Hogan, R. S. Lewis, A. Rao, Molecular basis of calcium signaling in lymphocytes: STIM and ORAI. *Annu. Rev. Immunol.* **28**, 491 (2010). doi:10.1146/annurev.immunol.021908.132550 Medline

2. J. Roos *et al*., STIM1, an essential and conserved component of store-operated Ca^{2+} channel function. *J. Cell Biol.* **169**, 435 (2005). doi:10.1083/jcb.200502019 Medline

3. S. L. Zhang *et al*., STIM1 is a Ca^{2+} sensor that activates CRAC channels and migrates from the Ca^{2+} store to the plasma membrane. *Nature* **437**, 902 (2005). doi:10.1038/nature04147 Medline

4. J. Liou *et al*., STIM is a Ca^{2+} sensor essential for Ca^{2+}-store-depletion-triggered Ca^{2+} influx. *Curr. Biol.* **15**, 1235 (2005). doi:10.1016/j.cub.2005.05.055 Medline

5. S. Feske *et al*., A mutation in Orai1 causes immune deficiency by abrogating CRAC channel function. *Nature* **441**, 179 (2006). doi:10.1038/nature04702 Medline

6. M. Vig *et al*., CRACM1 is a plasma membrane protein essential for store-operated Ca^{2+} entry. *Science* **312**, 1220 (2006). doi:10.1126/science.1127883 Medline

7. S. L. Zhang *et al*., Genome-wide RNAi screen of Ca^{2+} influx identifies genes that regulate Ca^{2+} release-activated Ca^{2+} channel activity. *Proc. Natl. Acad. Sci. U.S.A.* **103**, 9357 (2006). doi:10.1073/pnas.0603161103 Medline

8. A. V. Yeromin *et al*., Molecular identification of the CRAC channel by altered ion selectivity in a mutant of Orai. *Nature* **443**, 226 (2006). doi:10.1038/nature05108 Medline

9. M. Prakriya *et al*., Orai1 is an essential pore subunit of the CRAC channel. *Nature* **443**, 230 (2006). doi:10.1038/nature05122 Medline

10. M. Vig *et al*., CRACM1 multimers form the ion-selective pore of the CRAC channel. *Curr. Biol.* **16**, 2073 (2006). doi:10.1016/j.cub.2006.08.085 Medline

11. Single-letter abbreviations for the amino acid residues are as follows: A, Ala; C, Cys; D, Asp; E, Glu; F, Phe; G, Gly; H, His; I, Ile; K, Lys; L, Leu; M, Met; N, Asn; P, Pro; Q, Gln; R, Arg; S, Ser; T, Thr; V, Val; W, Trp; and Y, Tyr.

12. S. Carrasco, T. Meyer, STIM proteins and the endoplasmic reticulum-plasma membrane junctions. *Annu. Rev. Biochem.* **80**, 973 (2011). doi:10.1146/annurev-biochem-061609-165311 Medline

13. B. A. McNally, M. Yamashita, A. Engh, M. Prakriya, Structural determinants of ion permeation in CRAC channels. *Proc. Natl. Acad. Sci. U.S.A.* **106**, 22516 (2009). doi:10.1073/pnas.0909574106 Medline

14. Y. Zhou, S. Ramachandran, M. Oh-Hora, A. Rao, P. G. Hogan, Pore architecture of the ORAI1 store-operated calcium channel. *Proc. Natl. Acad. Sci. U.S.A.* **107**, 4896 (2010). doi:10.1073/pnas.1001169107 Medline

15. A. Penna *et al*., The CRAC channel consists of a tetramer formed by Stim-induced dimerization of Orai dimers. *Nature* **456**, 116 (2008). doi:10.1038/nature07338 Medline

16. W. Ji *et al*., Functional stoichiometry of the unitary calcium-release-activated calcium channel. *Proc. Natl. Acad. Sci. U.S.A.* **105**, 13668 (2008). doi:10.1073/pnas.0806499105 Medline

17. O. Mignen, J. L. Thompson, T. J. Shuttleworth, Orai1 subunit stoichiometry of the mammalian CRAC channel pore. *J. Physiol.* **586**, 419 (2008). doi:10.1113/jphysiol.2007.147249 Medline

18. A. Demuro *et al*., Subunit stoichiometry of human Orai1 and Orai3 channels in closed and open states. *Proc. Natl. Acad. Sci. U.S.A.* **108**, 17832 (2011). doi:10.1073/pnas.1114814108 Medline

19. M. Hoth, R. Penner, Calcium release-activated calcium current in rat mast cells. *J. Physiol.* **465**, 359 (1993). Medline

20. A. Lepple-Wienhues, M. D. Cahalan, Conductance and permeation of monovalent cations through depletion-activated Ca^{2+} channels (ICRAC) in Jurkat T cells. *Biophys. J.* **71**, 787 (1996). doi:10.1016/S0006-3495(96)79278-0 Medline

21. C. Aussel, R. Marhaba, C. Pelassy, J. P. Breittmayer, Submicromolar La^{3+} concentrations block the calcium release-activated channel, and impair CD69 and CD25 expression in $CD3^-$ or thapsigargin-activated Jurkat cells. *Biochem. J.* **313**, 909 (1996). Medline

22. A. V. Yeromin, J. Roos, K. A. Stauderman, M. D. Cahalan, A store-operated calcium channel in *Drosophila* S2 cells. *J. Gen. Physiol.* **123**, 167 (2004). doi:10.1085/jgp.200308982 Medline

23. Z. Li *et al*., Mapping the interacting domains of STIM1 and Orai1 in Ca^{2+} release-activated Ca^{2+} channel activation. *J. Biol. Chem.* **282**, 29448 (2007). doi:10.1074/jbc.M703573200 Medline

24. C. Y. Park *et al*., STIM1 clusters and activates CRAC channels via direct binding of a cytosolic domain to Orai1. *Cell* **136**, 876 (2009). doi:10.1016/j.cell.2009.02.014 Medline

25. Y. Zhou *et al*., STIM1 gates the store-operated calcium channel ORAI1 in vitro. *Nat. Struct. Mol. Biol.* **17**, 112 (2010). doi:10.1038/nsmb.1724 Medline

26. B. A. McNally, A. Somasundaram, M. Yamashita, M. Prakriya, Gated regulation of CRAC channel ion selectivity by STIM1. *Nature* **482**, 241 (2012). Medline

27. L. Navarro-Borelly *et al*., STIM1-Orai1 interactions and Orai1 conformational changes revealed by live-cell FRET microscopy. *J. Physiol.* **586**, 5383 (2008). doi:10.1113/jphysiol.2008.162503 Medline

28. M. Muik *et al*., Dynamic coupling of the putative coiled-coil domain of ORAI1 with STIM1 mediates ORAI1 channel activation. *J. Biol. Chem.* **283**, 8014 (2008). doi:10.1074/jbc.M708898200 Medline

29. I. Frischauf *et al*., Molecular determinants of the coupling between STIM1 and Orai channels: Differential activation of Orai1-3 channels by a STIM1 coiled-coil mutant. *J. Biol. Chem.* **284**, 21696 (2009). doi:10.1074/jbc.M109.018408 Medline

30. D. A. Doyle *et al*., The structure of the potassium channel: Molecular basis of K^+ conduction and selectivity. *Science* **280**, 69 (1998). doi:10.1126/science.280.5360.69 Medline

31. Aspartate residues on the disordered M1-M2 loop (D182 and D184, corresponding to D110 and D112 in Orai1) probably also contribute to the acidic nature of the extracellular mouth of the pore.

32. S. L. Zhang *et al*., Mutations in Orai1 transmembrane segment 1 cause STIM1-independent activation of Orai1 channels at glycine 98 and channel closure at arginine 91. *Proc. Natl. Acad. Sci. U.S.A.* **108**, 17838 (2011). doi:10.1073/pnas.1114821108 Medline

33. M. Hoth, Calcium and barium permeation through calcium release-activated calcium (CRAC) channels. *Pflugers Arch.* **430**, 315 (1995). doi:10.1007/BF00373905 Medline

34. Y. Zhou, J. H. Morais-Cabral, A. Kaufman, R. MacKinnon, Chemistry of ion coordination and hydration revealed by a K^+ channel-Fab complex at 2.0 Å resolution. *Nature* **414**, 43 (2001). doi:10.1038/35102009 Medline

35. A. Zweifach, R. S. Lewis, Mitogen-regulated Ca^{2+} current of T lymphocytes is activated by depletion of intracellular Ca^{2+} stores. *Proc. Natl. Acad. Sci. U.S.A.* **90**, 6295 (1993). doi:10.1073/pnas.90.13.6295 Medline

36. M. Prakriya, R. S. Lewis, Regulation of CRAC channel activity by recruitment of silent channels to a high open-probability gating mode. *J. Gen. Physiol.* **128**, 373 (2006). doi:10.1085/jgp.200609588 Medline

37. B. Hille, in *Ionic Channels of Excitable Membranes* (Sinauer Associates, Sunderland, MA, ed. 2, 1992), pp. xiii.

38. D. Bakowski, A. B. Parekh, Monovalent cation permeability and Ca^{2+} block of the store-operated Ca^{2+} current I_{CRAC} in rat basophilic leukemia cells. *Pflugers Arch.* **443**, 892 (2002). doi:10.1007/s00424-001-0775-8 Medline

39. B. D. James *et al*., The hexachloroferrate(III) anion stabilized in hydrogen bonded packing arrangements. A comparison of the x-ray crystal structures and low temperature magnetism of tetrakis (methylammonium) hexachloroferrate (III) chloride (I) and tetrakis (hexamethylenediammonium) hexachloroferrate (III) tetrachloroferrate (III) tetrachloride (II). *Inorg. Chim. Acta* **247**, 169 (1996). doi:10.1016/0020-1693(95)04955-X

40. I. Derler *et al*., Increased hydrophobicity at the N terminus/membrane interface impairs gating of the severe combined immunodeficiency-related ORAI1 mutant. *J. Biol. Chem.* **284**, 15903 (2009). doi:10.1074/jbc.M808312200 Medline

41. H. Kawasaki, R. H. Kretsinger, Calcium-binding proteins 1: EF-hands. *Protein Profile* **2**, 297 (1995). Medline

42. J. P. Yuan *et al*., SOAR and the polybasic STIM1 domains gate and regulate Orai channels. *Nat. Cell Biol.* **11**, 337 (2009). doi:10.1038/ncb1842 Medline

43. M. Muik *et al*., A cytosolic homomerization and a modulatory domain within STIM1 C terminus determine coupling to ORAI1 channels. *J. Biol. Chem.* **284**, 8421 (2009). doi:10.1074/jbc.C800229200 Medline

44. T. Kawasaki, I. Lange, S. Feske, A minimal regulatory domain in the C terminus of STIM1 binds to and activates ORAI1 CRAC channels. *Biochem. Biophys. Res. Commun.* **385**, 49 (2009).

45. A. Lis, S. Zierler, C. Peinelt, A. Fleig, R. Penner, A single lysine in the N-terminal region of store-operated channels is critical for STIM1-mediated gating. *J. Gen. Physiol.* **136**, 673 (2010). doi:10.1085/jgp.201010484 Medline

46. T. Kawate, E. Gouaux, Fluorescence-detection size-exclusion chromatography for precrystallization screening of integral membrane proteins. *Structure* **14**, 673 (2006). doi:10.1016/j.str.2006.01.013 Medline

47. J. V. Kilmartin, B. Wright, C. Milstein, Rat monoclonal antitubulin antibodies derived by using a new nonsecreting rat cell line. *J. Cell Biol.* **93**, 576 (1982). doi:10.1083/jcb.93.3.576 Medline

48. S. B. Long, E. B. Campbell, R. MacKinnon, Crystal structure of a mammalian voltage-dependent Shaker family K^+ channel. *Science* **309**, 897 (2005). doi:10.1126/science.1116269 Medline

49. Z. Otwinowski, W. Minor, Processing of x-ray diffraction data collected in oscillation mode. *Methods Enzymol.* **276**, 307 (1997). doi:10.1016/S0076-6879(97)76066-X

50. C. Vonrhein, E. Blanc, P. Roversi, G. Bricogne, Automated structure solution with autoSHARP. *Methods Mol. Biol.* **364**, 215 (2007). Medline

51. K. D. Cowtan, in *Joint CCP4 and ESF-EACBM Newsletter on Protein Crystallography*, no. 31 (1994), pp. 34–38.

52. T. A. Jones, J.-Y. Zou, S. W. Cowan, M. Kjeldgaard, Improved methods for building protein models in electron density maps and the location of errors in these models. *Acta Crystallogr. A* **47**, 110 (1991). doi:10.1107/S0108767390010224 Medline

53. P. Emsley, B. Lohkamp, W. G. Scott, K. Cowtan, Features and development of Coot. *Acta Crystallogr. D Biol. Crystallogr.* **66**, 486 (2010). doi:10.1107/S0907444910007493 Medline

54. A. T. Brünger *et al*., Crystallography & NMR system: A new software suite for macromolecular structure determination. *Acta Crystallogr. D Biol. Crystallogr.* **54**, 905 (1998). doi:10.1107/S0907444998003254 Medline

55. P. D. Adams *et al*., PHENIX: A comprehensive Python-based system for macromolecular structure solution. *Acta Crystallogr. D Biol. Crystallogr.* **66**, 213 (2010). doi:10.1107/S0907444909052925 Medline

56. O. S. Smart, J. G. Neduvelil, X. Wang, B. A. Wallace, M. S. Sansom, HOLE: A program for the analysis of the pore dimensions of ion channel structural models. *J. Mol. Graph.* **14**, 354, 376 (1996). doi:10.1016/S0263-7855(97)00009-X Medline

57. N. A. Baker, D. Sept, S. Joseph, M. J. Holst, J. A. McCammon, Electrostatics of nanosystems: Application to microtubules and the ribosome. *Proc. Natl. Acad. Sci. U.S.A.* **98**, 10037 (2001). doi:10.1073/pnas.181342398 Medline

58. L. Heginbotham, L. Kolmakova-Partensky, C. Miller, Functional reconstitution of a prokaryotic K^+ channel. *J. Gen. Physiol.* **111**, 741 (1998). doi:10.1085/jgp.111.6.741 Medline

59. J. Zhang, Y. Feng, M. Forgac, Proton conduction and bafilomycin binding by the V0 domain of the coated vesicle V-ATPase. *J. Biol. Chem.* **269**, 23518 (1994). Medline

60. S.-Y. Lee, J. A. Letts, R. MacKinnon, Functional reconstitution of purified human Hv1 H^+ channels. *J. Mol. Biol.* **387**, 1055 (2009). doi:10.1016/j.jmb.2009.02.034 Medline

61. L. Feng, E. B. Campbell, Y. Hsiung, R. MacKinnon, Structure of a eukaryotic CLC transporter defines an intermediate state in the transport cycle. *Science* **330**, 635 (2010). doi:10.1126/science.1195230 Medline

62. A. N. Miller, S. B. Long, Crystal structure of the human two-pore domain potassium channel K2P1. *Science* **335**, 432 (2012). doi:10.1126/science.1213274 Medline

63. Y. Hayashi, H. Matsui, T. Takagi, Membrane protein molecular weight determined by low-angle laser light-scattering photometry coupled with high-performance gel chromatography. *Methods Enzymol.* **172**, 514 (1989). doi:10.1016/S0076-6879(89)72031-0 Medline

64. D. Yernool, O. Boudker, E. Folta-Stogniew, E. Gouaux, Trimeric subunit stoichiometry of the glutamate transporters from *Bacillus caldotenax* and *Bacillus stearothermophilus*. *Biochemistry* **42**, 12981 (2003). doi:10.1021/bi030161q Medline

65. E. Folta-Stogniew, Oligomeric states of proteins determined by size-exclusion chromatography coupled with light scattering, absorbance, and refractive index detectors. *Methods Mol. Biol.* **328**, 97 (2006). Medline

66. E. Folta-Stogniew, K. R. Williams, Determination of molecular masses of proteins in solution: Implementation of an HPLC size exclusion chromatography and laser light scattering service in a core laboratory. *J. Biomol. Tech.* **10**, 51 (1999). Medline

67. J. A. Ballesteros, X. Deupi, M. Olivella, E. E. Haaksma, L. Pardo, Serine and threonine residues bend α-helices in the $\chi_1 = g^-$ conformation. *Biophys. J.* **79**, 2754 (2000). doi:10.1016/S0006-3495(00)76514-3 Medline

68. Y. Jiang *et al*., The open pore conformation of potassium channels. *Nature* **417**, 523 (2002). doi:10.1038/417523a Medline

69. A. Alam, Y. Jiang, High-resolution structure of the open NaK channel. *Nat. Struct. Mol. Biol.* **16**, 30 (2008). doi:10.1038/nsmb.1531 Medline